Computer Modeling in
Engineering & Sciences

Tech Science Press

https://doi.org/10.32604/cmes.2026.085279

ARTICLE

DLPC-GNN A Dual-Layer Progressive Physics-Constrained Graph Neural Network for Asphalt Pavement Distress Prediction and Maintenance Strategy Classification

Mengyao Wang[1], Ailian Zhu[2], Longji Zhu[3,*], Chen Lan[4,*] and Yang Li[5]

[1]School of Civil Engineering and Transportation Engineering, Yellow River Conservancy Technical University, Kaifeng, China
[2]Huishen (Yantian) Expressway Huizhou Company Limited, Huizhou, China
[3]Jiangxi Province Key Laboratory of Environmental Geotechnical Engineering and Hazards Control, Jiangxi University of Science and Technology, Ganzhou, China
[4]School of Business Administration, Heyuan Polytechnic, Heyuan, China
[5]School of Civil Engineering and Architecture, Henan University, Kaifeng, China

*Corresponding Authors: Longji Zhu. Email: zhu.longji@jxust.edu.cn; Chen Lan. Email: chen_lan_work@126.com

Received: 08 May 2026; Accepted: 06 August 2026; Published: 28 August 2026

ABSTRACT: Accurate prediction of asphalt pavement distress is essential for proactive maintenance and life-cycle infrastructure management. However, existing data-driven methods often struggle to jointly represent multi-source inspection data, distress evolution mechanisms, and spatial propagation relationships among pavement sections. To address these limitations, this study proposes a Dual-Layer Progressive Physics-Constrained Graph Neural Network (DLPC-GNN) for asphalt pavement distress prediction and maintenance strategy classification. The proposed model represents pavement deterioration using a dual-layer graph structure. At the microscopic level, cracks, surface deterioration, and structural moisture-induced damage are modeled as physically associated distress nodes. At the macroscopic level, pavement-section supernodes are connected according to spatial distance, traffic-flow correlation, and structural continuity. To improve physical consistency and interpretability, seepage, fatigue crack growth, hydrodynamic pressure, and bounded deflection evolution mechanisms are incorporated into physics-informed edge initialization and auxiliary physical constraints. The model is validated using multi-source inspection data from the Huizhou section of the Huizhou–Shenzhen Expressway. Experimental results show that DLPC-GNN outperforms conventional machine learning models, deep learning models, and purely data-driven graph neural networks in both continuous distress-state prediction and maintenance strategy classification. For the continuous distress-state regression task, DLPC-GNN achieves an MAE of 2.78 and an RMSE of 4.62. For the maintenance strategy classification task, it achieves a Recall of 88.8%. Compared with the purely data-driven GNN, DLPC-GNN reduces MAE and RMSE by 15.1% and 21.4%, respectively, and improves Recall by 12.2%. Ablation and robustness analyses further demonstrate that the dual-layer graph structure, physics-informed edge initialization, and physical constraints improve prediction stability under small-sample, noisy, and feature-missing conditions. These results indicate that DLPC-GNN provides a physics-guided and partially interpretable graph-learning framework for maintenance-oriented asphalt pavement distress assessment.

KEYWORDS: Asphalt pavement; graph neural network; physics-constrained learning; distress evolution; hydro-mechanical coupling; maintenance strategy classification

Copyright © 2026 The Authors. Published by Tech Science Press. This work is licensed under a Creative Commons Attribution 4.0 International License, which permits unrestricted use, distribution, and reproduction in any medium, provided the original work is properly cited.

1 Introduction

Asphalt pavement is one of the most widely used pavement structures in highway and urban road systems, and its service performance is directly related to traffic safety, transportation efficiency, and the life-cycle economy of infrastructure. In recent years, with the continuous increase in traffic loading, the more frequent occurrence of extreme rainfall events, and the prolonged service life of pavement structures, asphalt pavements have become increasingly susceptible to the coupled effects of vehicular loading, environmental temperature–humidity cycles, rainfall infiltration, and material aging. These factors gradually induce multiple types of pavement distresses, including cracking, rutting, potholes, raveling, settlement, and structural moisture-induced damage [1]. If early-stage distresses cannot be accurately identified and proactively maintained, local surface damage may progressively propagate into the structural layers, further triggering base-course voiding, interlayer bonding failure, and degradation of overall bearing capacity, ultimately resulting in substantially increased maintenance costs and shortened pavement service life. Therefore, accurately characterizing the spatiotemporal evolution of pavement distresses from multi-source inspection data and developing an engineering-interpretable maintenance decision-making model have become critical issues in intelligent operation and maintenance of road infrastructure.

Traditional pavement distress detection and maintenance decision-making methods mainly rely on manual inspection, empirical judgment, and index-threshold-based evaluation. Manual visual inspection and field surveys can directly capture surface distress information; however, they are inefficient, labor-intensive, and highly dependent on inspectors' experience and subjective judgment, making them difficult to satisfy the requirements of rapid large-scale road-network inspection and refined maintenance management [2,3]. Evaluation methods based on pavement condition indices, roughness, deflection, skid resistance, and other indicators have been widely used in engineering practice. Nevertheless, such methods usually rely on a single indicator or a limited number of indicators for decision-making and mainly reflect the current pavement condition, while failing to reveal the interaction mechanisms among different distress types and their future evolution trends. In particular, with the increasing availability of multi-source inspection data, conventional threshold-based and expert-experience-based methods cannot fully exploit heterogeneous information such as images, deflection measurements, ground-penetrating radar data, traffic loading, rainfall environment, and material parameters. As a result, maintenance decision-making still suffers from delayed response, local optimization, and insufficient interpretability [4].

With the development of automated inspection equipment and computer vision techniques, image-processing- and deep-learning-based pavement distress recognition methods have made significant progress. Traditional image processing methods can identify surface distresses such as cracks and potholes through edge detection, texture analysis, and morphological filtering. Furthermore, convolutional neural networks and their improved variants can automatically extract high-dimensional image features and have achieved high accuracy in crack detection, pothole recognition, and distress classification tasks [5,6]. In recent years, three-dimensional reconstruction, RGB-D cameras, infrared thermography, binocular vision, and semi-supervised segmentation techniques have also been introduced into pavement distress recognition, enabling models to extend from two-dimensional texture features to three-dimensional geometric morphology, thermal anomalies, and distress identification under weakly annotated scenarios [7–10]. In addition, binocular-vision-based pothole detection systems and large-scale pavement image databases have further promoted the development of pavement distress recognition from single-image classification toward three-dimensional measurement, automatic annotation, and deterioration trend prediction [11,12].

However, most existing vision-driven methods focus on the static recognition of apparent pavement distresses. Their core objective is usually to "detect" and "classify" distress rather than to explain why distress occurs, how it propagates, and where it will evolve. For asphalt pavements, there are significant physical coupling relationships among crack propagation, moisture infiltration, base weakening, hydrodynamic scouring, and surface deterioration. For example, once cracks damage the waterproof continuity of the surface layer, preferential seepage channels may form, allowing rainfall to more easily enter the pavement structure. Under traffic loading, infiltrated water may further generate hydrodynamic pressure and scouring effects, inducing base loosening, pumping, and local voiding. The reduction in structural bearing capacity then further accelerates surface deterioration and crack propagation. If prediction relies only on images or statistical correlations, the model may easily overlook the hydro-mechanical coupling mechanism underlying distress propagation, thereby compromising the reliability of long-term prediction and the proactiveness of maintenance decision-making.

In recent years, machine learning and deep learning methods have been widely applied to pavement performance prediction and maintenance decision optimization. Support vector machines, random forests, gradient boosting trees, recurrent neural networks, and deep learning models can learn nonlinear mapping relationships from historical inspection data and have been used to predict pavement roughness, deflection, cracking ratio, pavement condition index, or maintenance strategy categories [13–15]. Compared with traditional empirical models, data-driven approaches have clear advantages in extracting complex nonlinear features and can, to some extent, improve long-term pavement performance prediction and maintenance resource allocation efficiency [16,17]. Furthermore, reinforcement learning, random forests, XGBoost, image-segmentation-assisted multi-criteria decision-making, and multi-objective optimization methods have been applied to maintenance planning, crack-cause identification, and sustainable maintenance decision-making, providing new technical pathways for the transition from experience-driven maintenance to intelligent decision-making [18–21].

Nevertheless, these models usually treat pavement distress samples as independent data points, making it difficult to represent the spatial continuity among pavement sections and the structural associations among distress types. In addition, the parameter learning of purely data-driven models mainly depends on the distribution of training samples. When the number of samples is limited, inspection noise is high, or the external environment changes significantly, their generalization capability may deteriorate. Moreover, deep learning models generally suffer from the "black-box" problem, and their prediction results are difficult to associate with explicit mechanical mechanisms, material boundaries, and distress evolution laws. This limitation restricts their application in high-reliability engineering maintenance decision-making.

Graph neural networks provide a new modeling paradigm for describing spatial correlations and topological propagation in pavement distresses. Unlike convolutional neural networks, which mainly process regular grid data, graph neural networks perform message passing and neighborhood aggregation on non-Euclidean graph structures. They are therefore suitable for representing traffic correlations among pavement sections, structural continuity, and complex dependencies among distress nodes. In transportation engineering, graph neural networks have been widely used for traffic flow prediction, road-network state estimation, travel demand prediction, and traffic incident detection, demonstrating stronger spatial modeling capability than conventional sequence models [22,23]. For pavement distress maintenance, graph neural networks offer the potential to treat cracks, moisture-induced damage, and surface deterioration as microscopic nodes and adjacent pavement sections as macroscopic topological nodes, thereby simultaneously characterizing local distress coupling relationships and regional deterioration propagation patterns. Existing studies have begun to explore the application of digital twins and graph neural networks in pavement health monitoring and maintenance optimization, providing new graph-based modeling frameworks for pavement structural condition perception and maintenance strategy optimization [24]. However, most existing studies construct graph structures using distance thresholds, statistical correlations, or empirical adjacency matrices. The resulting edge weights lack explicit physical meaning and cannot sufficiently reflect engineering mechanisms such as crack-induced infiltration, hydrodynamic scouring, and fatigue crack growth. Therefore, constructing graph structures with physical interpretability remains one of the core challenges in applying graph neural networks to pavement distress prediction and maintenance decision-making.

Physics-informed neural networks provide an effective approach for addressing the insufficient physical consistency of deep learning models. Such methods embed governing equations, boundary conditions, initial conditions, or material constitutive relationships into loss functions, enabling neural networks to satisfy fundamental physical laws while fitting data. In recent years, physics-informed neural networks have been applied in fluid mechanics, solid mechanics, structural dynamics, material parameter inversion, and structural health monitoring, showing potential for reducing data requirements, improving generalization capability, and enhancing interpretability [25,26]. Furthermore, physics-informed graph neural networks and graph neural networks incorporating physical loss functions have been used for predicting mechanical responses of complex structures and materials. These studies indicate that combining graph-structure representation with physical constraints can improve the ability of models to characterize the mechanical behavior of irregular structural systems [27,28]. Relevant reviews have also pointed out that physics-informed neural networks are gradually expanding from conventional continuous-field solutions to broader scenarios, including structural engineering, material modeling, and complex engineering system prediction [29,30]. For asphalt pavement distress evolution, existing studies have started to introduce physics-informed deep learning into pavement crack prediction, indicating that embedding crack evolution mechanisms into neural networks can improve the physical consistency of pavement performance prediction [4]. However, traditional physics-informed neural networks are mostly used for solving continuous physical fields in regular domains, whereas pavement distress data are often multi-source, heterogeneous, discrete, and characterized by complex topological relationships. How to organically integrate physical equation constraints with the message-passing mechanism of graph neural networks still lacks systematic investigation.

Based on the above analysis, this study argues that a pavement distress maintenance decision-making model should not only be capable of extracting nonlinear features from multi-source inspection data, but should also simultaneously represent the physical evolution relationships among distresses, the spatial topological dependencies among pavement sections, and the mechanical rationality of prediction results. To this end, this paper proposes a Dual-Layer Progressive Physics-Constrained Graph Neural Network for asphalt pavement distress-state prediction and maintenance decision classification. The proposed model employs graph structures as a unified representation framework. At the microscopic level, a distress-oriented physical association graph composed of cracks, structural moisture-induced damage, and surface deterioration is constructed to describe local hydro-mechanical coupling mechanisms, including rainfall infiltration, hydrodynamic scouring, and fatigue crack propagation. Existing studies have shown that moisture-induced damage in asphalt mixtures involves complex processes such as moisture migration, pore-structure evolution, hydrodynamic pressure impact, and mesoscopic damage accumulation [31–34]. Under the combined action of traffic loading and moisture, dynamic stress and excess pore-water pressure responses may also occur inside pavement structures, further aggravating material damage and structural performance deterioration [35].

At the macroscopic level, this study constructs a road-network topology graph that integrates spatial distance, traffic-flow correlation, and structural continuity to characterize regional distress propagation among adjacent pavement sections. Furthermore, the Richards equation for unsaturated seepage, the Paris law for fatigue crack growth, a hydrodynamic pressure model, and a bounded deflection evolution model are introduced for physics-informed edge initialization. Based on theoretical foundations such as fatigue life prediction of asphalt mixtures and viscoelastic continuum damage models, a multi-source physics-constrained loss function is further developed by incorporating mechanical response constraints, material boundary constraints, and evolutionary logic constraints, thereby improving the prediction accuracy, physical consistency, and engineering interpretability of the model [36,37].

The primary objective of this study is to develop and validate an engineering-interpretable graph-learning framework for asphalt pavement distress-state prediction and maintenance decision-making by integrating multi-source inspection data, distress evolution mechanisms, road-network spatial topology, and physics-based constraints. Specifically, this study aims to: (i) formulate pavement distress evolution as a dual-layer graph-sequence prediction problem involving both microscopic distress interactions and macroscopic inter-section propagation; (ii) embed hydro-mechanical and fracture-mechanics-based physical priors into graph edge initialization and model training; and (iii) evaluate whether the proposed framework can improve prediction accuracy, physical consistency, robustness, and maintenance decision reliability under practical inspection conditions. The overall research framework and technical route of the proposed DLPC-GNN are illustrated in Fig. 1.

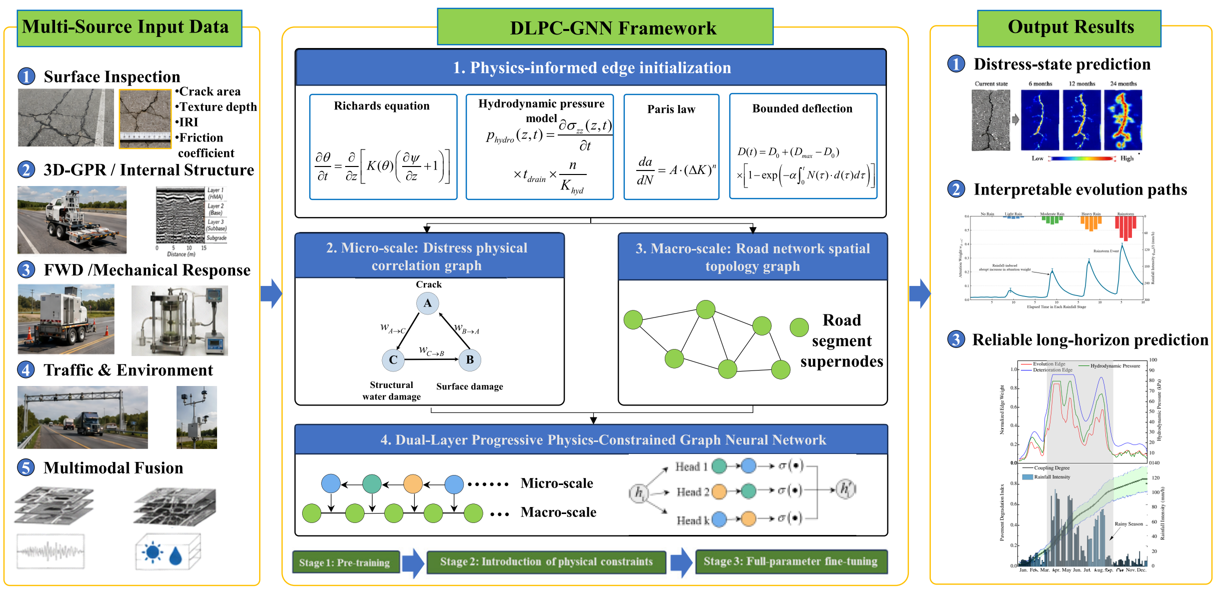

Figure 1: The Dual-layer progressive physics-constrained graph neural network for asphalt pavement distress-state prediction and maintenance strategy classification.

To clarify how the above objective is achieved, the main contributions of this study are summarized as follows:

(1) A Dual-Layer progressive graph-structure modeling framework is proposed for asphalt pavement distress maintenance decision-making. The framework characterizes the physical coupling relationships among cracks, structural moisture-induced damage, and surface deterioration at the microscopic level, while representing the topological dependencies among pavement sections jointly determined by spatial distance, traffic flow, and structural continuity at the macroscopic level. This enables multi-scale modeling of pavement distress evolution from local deterioration to regional propagation.

(2) A physics-based edge-weight initialization method is proposed. Unlike conventional graph neural networks that construct adjacency matrices based on distance or statistical correlations, this study calculates distress association intensities using physical models related to unsaturated seepage, fatigue crack growth, hydrodynamic pressure, and structural bearing-capacity degradation. As a result, the edge weights in the graph structure have explicit engineering significance.

(3) A multi-source physics-constrained joint loss function is constructed. By introducing mechanical response constraints, material boundary constraints, and evolutionary logic constraints, the network training process not only pursues data-fitting accuracy but also satisfies mechanical boundaries, material parameter ranges, and distress propagation laws during pavement structural deterioration. This enhances the interpretability and generalization capability of the model.
(4) A progressive training strategy is designed to improve the optimization stability of the physics-constrained graph neural network. Through a training process consisting of data warm-up, physical-rule introduction, and full-parameter fine-tuning, the increased non-convexity of the loss landscape caused by multi-source physical constraints can be alleviated, thereby improving model convergence stability.
(5) Multi-source inspection data from the Huizhou section of the Huizhou–Shenzhen Expressway are used for validation. Through baseline model comparison, physical consistency analysis, ablation experiments, and robustness tests under non-ideal data conditions, the comprehensive performance of DLPC-GNN is systematically evaluated in terms of distress-state prediction, maintenance decision classification, physical mechanism representation, and engineering applicability.

The remainder of this paper is organized as follows. Section 2 introduces the graph-structure representation of pavement structural distresses and the related physical models. Section 3 presents the architecture of DLPC-GNN, the multi-source physics-constrained loss function, and the progressive training strategy. Section 4 describes the engineering dataset, model training settings, and evaluation metrics. Section 5 reports and discusses the experimental results, including prediction accuracy comparison, physical consistency validation, ablation experiments, and robustness analysis. Section 6 is the discussion of the analysis results and the model. Section 7 concludes the paper and outlines future research directions.

2 Graph-Based Representation of Pavement Structural Distresses

2.1 Time-Series Definition of the Structural Deterioration Problem

During service, asphalt pavement structures are subjected to the long-term coupled effects of traffic-induced dynamic loading and environmental hydrothermal actions. Consequently, their mechanical performance exhibits significant time-dependent deterioration characteristics. Conventional static evaluation methods are insufficient for capturing the dynamic propagation process of pavement distresses. Therefore, this study formulates pavement distress evolution as a graph-sequence prediction problem at discrete time steps. Given a time-series graph dataset containing multi-source inspection data, denoted as $D = \{G_1, G_2, \ldots, G_T\}$, where G_t represents the spatial state of the pavement structure at time t, including local distress features and global mechanical parameters, the core objective of this study is to construct an end-to-end nonlinear mapping function f_θ. This function is designed to predict the physical topological state $\hat{G}_{t+\Delta t}$ of the pavement structure at time $t + \Delta t$, together with the corresponding optimal maintenance strategy $\hat{y}_{\mathrm{maintenance}}$:

$$f_\theta: G_t \rightarrow \left(\hat{y}_{maintenance}, \hat{G}_{t+\Delta t}\right) \tag{1}$$

2.2 Dual-Layer Progressive Spatial Topology-Aware Graph Structure

Pavement structural failure is not an isolated event but a multi-scale evolution process that spans from microscopic material damage to macroscopic structural degradation. To accurately perceive such spatial topological relationships, this study develops a Dual-Layer progressive graph structure.

2.2.1 Microscopic Layer: Distress-Oriented Physical Association Graph Based on Hydro-Mechanical Coupling

At the microscopic level, cracking, moisture-induced damage, and surface deterioration exhibit strong nonlinear physical feedback mechanisms. Purely data-driven random graph construction methods may disconnect these inherent physical relationships. The nonlinear physical feedback mechanism among cracking, structural moisture-induced damage, and surface deterioration is illustrated in Fig. 2.

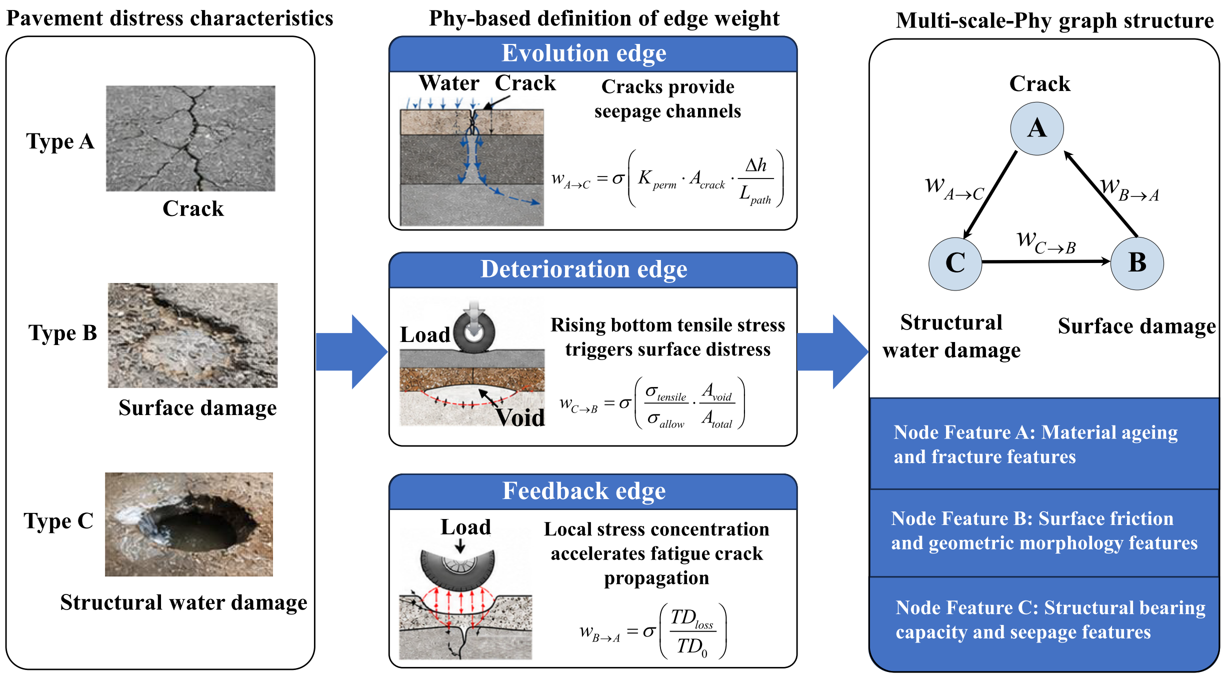

Figure 2: Nonlinear physical feedback mechanism among cracks, water damage and surface damage.

Therefore, this study defines three typical types of distresses as graph nodes and determines their node features and directed edge weights based on principles of soil mechanics and fracture mechanics. Specifically, the typical distress nodes are divided into three categories: type-A nodes, namely cracking-related nodes, focus on material aging and fracture characteristics x_A; type-B nodes, namely surface deterioration nodes, focus on surface friction and geometric morphology x_B; and type-C nodes, namely structural moisture-induced damage nodes, focus on structural bearing capacity and water infiltration characteristics x_C. Based on these typical distress categories, three types of directed edges are constructed.

Evolution edge A → C: crack-induced moisture damage. Surface cracks disrupt the waterproof continuity of the pavement surface layer and provide preferential seepage channels for rainfall infiltration. Considering the gravity-driven infiltration mechanism of water through cracks, the edge weight should be positively correlated with the crack opening area and the seepage driving force, namely the hydraulic head gradient. Therefore, the corresponding edge weight is defined as:

$$w_{\mathrm{A}\to\mathrm{C}} = \sigma\left(K_{\mathrm{perm}}\cdot A_{\mathrm{crack}}\cdot\frac{\Delta h}{L_{\mathrm{path}}}\right) \tag{2}$$

where $\sigma(\cdot)$ denotes the sigmoid activation function, which normalizes the physical quantity into the network weight space; A_{crack} is the crack area; Δh is the hydraulic head difference; and L_{path} is the seepage path length.

In the practical implementation, the scalar parameters in Eq. (2) are extracted from the discretized monitoring section rather than directly solved from a continuous seepage field. For the i-th pavement section at time step t, the permeability-related parameter $K_{\mathrm{perm}}^{i,t}$ is defined as the equivalent unsaturated hydraulic conductivity along the dominant infiltration path from the pavement surface to the moisture-sensitive structural layer. Since the seepage path usually passes through multiple pavement layers with different hydraulic properties, a thickness-weighted harmonic average is adopted:

$$K_{\mathrm{perm}}^{i,t} = \left[\frac{1}{L_{\mathrm{path}}^{i}} \sum_{l=1}^{n_l} \frac{H_l^i}{K_l\left(\theta_l^{i,t}\right) + \varepsilon} \right]^{-1} \tag{3}$$

where H_l^i is the thickness of the l-th layer in the i-th pavement section, $K_l\left(\theta_l^{i,t}\right)$ is the unsaturated hydraulic conductivity of this layer under the moisture state $\theta_l^{i,t}$, n_l is the number of layers crossed by the infiltration path, and ε is a small numerical constant used to avoid division by zero. The saturated hydraulic conductivity of each layer is obtained from constant-head or falling-head permeability tests, while the moisture state is updated using time-domain reflectometry measurements. Therefore, $K_{\mathrm{perm}}^{i,t}$ represents a section-level equivalent scalar extracted from the layer-wise hydrological field, making it suitable for graph edge initialization.

The crack opening area $A_{\mathrm{crack}}^{i,t}$ is quantified from automated pavement detection images. The pavement image of each monitoring section is first mapped to real-world coordinates according to the camera calibration parameters and laser profiler resolution. Crack pixels are then extracted from the binary crack mask, and the crack area is calculated as

$$A_{\mathrm{crack}}^{i,t} = \sum_{p \in \Omega_{\mathrm{i}}} M_{\mathrm{crack}}^{i,t}(p)\Delta x \Delta y \tag{4}$$

where $M_{\mathrm{crack}}^{i,t}(p)$ is the crack mask value of pixel p, Ω_{i} denotes the image region corresponding to the i-th pavement section, and Δx and Δy are the physical pixel resolutions in the longitudinal and transverse directions, respectively. When line-laser depth information is available, the extracted crack area is further checked using the measured crack width and crack length to reduce the influence of surface stains and shadows.

The hydraulic head difference $\Delta h^{i,t}$ is determined by the rainfall boundary condition and the internal moisture state of the pavement structure. The rainfall intensity R_t is first converted into rainfall flux q_r^t. Considering that only the effective infiltrating rainfall contributes to crack-induced seepage, the effective infiltration flux is expressed as $q_{\mathrm{eff}}^{i,t} = \xi_i R_t$, where ξ_i is a runoff–infiltration coefficient related to surface texture, drainage condition, and crack connectivity. The equivalent surface water head is then estimated by

$$h_s^{i,t} = \frac{q_{\mathrm{eff}}^{i,t}}{K_{\mathrm{perm}}^{i,t} + \varepsilon} L_{\mathrm{path}}^{i} \tag{5}$$

and the hydraulic head difference is calculated as

$$\Delta h^{i,t} = \max\left(h_s^{i,t} - h_b^{i,t}, 0\right) \tag{6}$$

where $h_b^{i,t}$ denotes the equivalent internal water head derived from groundwater-level and subgrade-moisture measurements. The max operator is used to ensure that the edge intensity is activated only when the surface rainfall boundary provides a positive downward infiltration driving force.

The seepage path length L_{path}^{i} is determined according to the pavement structural configuration and the target moisture-sensitive layer. For dry sections, it is calculated as the cumulative thickness from the pavement surface to the top of the semi-rigid base layer. For medium-moisture sections with an additional cushion layer, the path length is extended to the layer where moisture accumulation or voiding is detected by three-dimensional ground-penetrating radar (3D-GPR). Thus,

$$L_{\text{path}}^{i} = \sum_{l=1}^{n_l} H_l^i \tag{7}$$

Finally, $K_{\text{perm}}^{i,t}$, $A_{\text{crack}}^{i,t}$, $\Delta h^{i,t}$, and L_{path}^{i} are normalized using the training-set statistics before being substituted into Eq. (2). This procedure converts the distributed seepage-related information into a reproducible scalar edge weight for the crack-induced moisture-damage edge.

Deterioration edge C → B: moisture-induced weakening of structural bearing capacity. After water infiltrates into the base layer, pumping and voiding may occur under repeated traffic loading, leading to the loss of support beneath the surface layer. According to elastic layered system theory, voiding sharply increases the tensile stress at the bottom of the structural layer, thereby inducing more severe surface deterioration. To quantify this mechanically driven deterioration process, the ratio of actual tensile stress to allowable tensile stress and the void-area proportion are used to characterize the edge weight:

$$w_{\text{C}\to\text{B}} = \sigma\left(\frac{\sigma_{\text{tensile}}}{\sigma_{\text{allow}}} \cdot \frac{A_{\text{void}}}{A_{\text{total}}}\right) \tag{8}$$

where σ_{tensile} denotes the tensile stress at the bottom of the structural layer; σ_{allow} denotes the allowable tensile stress of the material; and A_{void} and A_{total} represent the void area and total area, respectively.

Feedback edge B → A: surface deterioration accelerating crack propagation. The degradation of surface texture depth, such as rutting and pothole formation, changes the tire–pavement contact stress distribution and induces local stress concentration, thereby reversely accelerating the fatigue propagation of existing cracks. The intensity of this feedback mechanism is determined by the relative loss ratio of texture depth:

$$w_{\text{B}\to\text{A}} = \sigma\left(\frac{TD_{\text{loss}}}{TD_0}\right) \tag{9}$$

where TD_{loss} denotes the loss of texture depth, and TD_0 is the texture depth in the initial state.

2.2.2 Macroscopic Layer: Road-Network Spatial Topology Graph Incorporating Structural Continuity

At the macroscopic level, adjacent pavement sections exhibit high continuity in terms of traffic flow distribution and underlying geological structure. In this study, the microscopic distress graph is pooled into macroscopic pavement-section supernodes $H_{\text{road}}^{(i)}$. The spatial dependency weight between pavement sections is then calculated by integrating multiple factors:

$$w_{ij}^{\text{spatial}} = \text{softmax}_{j\in \text{N}(i)}\left(\alpha e^{-d_{ij}/L_0} + \beta T_{ij} + \gamma S_{ij}\right) \tag{10}$$

For each source section i, the softmax operation in Eq. (10) is evaluated over all candidate neighbors $j\in\text{N}(i)$. This formulation incorporates the physical distance decay term e^{-d_{ij}/L_0}, the traffic-flow correlation intensity T_{ij}, and the structural continuity indicator S_{ij}, ensuring that the network can capture the propagation tendency of pavement distresses along traffic-flow directions and weak geological zones.

2.2.3 Explicit Graph Construction Protocol

To make the graph construction process reproducible, the node definition, microscopic-to-macroscopic mapping, edge thresholding, and edge-weight normalization procedures are clarified in this subsection.

For each observation time step (t), one dual-layer graph snapshot ($G_t = (G_t^{micro}, G_t^{macro})$) is constructed. The investigated expressway section has a total length of 32.191 km. In the implemented dataset, each macroscopic pavement-section supernode corresponds to a physical monitoring section of approximately 500 m in length, covering all lanes in one traffic direction. Considering the two travel directions, each graph snapshot contains ($\mathrm{N_s} = 130$) macroscopic pavement-section supernodes. Within each macroscopic supernode, three microscopic distress nodes are defined, namely a cracking-related node, a surface-deterioration node, and a structural moisture-induced damage node. Therefore, each graph snapshot contains ($3N_s = 390$) microscopic distress nodes and ($\mathrm{N_s} = 130$) macroscopic supernodes.

The microscopic-to-macroscopic mapping is performed at the pavement-section level. For the (i)-th pavement section, the three microscopic distress nodes $\left(v_i^A, v_i^B, v_i^C\right)$ are aggregated into the corresponding macroscopic supernode through the attention pooling operation described in Eq. (22). This design allows the macroscopic supernode to represent the section-level deterioration state learned from the local coupling among cracking, surface deterioration, and structural moisture-induced damage, rather than being a simple geometric aggregation unit.

For the microscopic graph, three directed physical candidate edges are constructed within each pavement section: $\left(v_i^A \to v_i^C\right)$, $\left(v_i^C \to v_i^B\right)$, and $\left(v_i^B \to v_i^A\right)$. These edges represent crack-induced rainfall infiltration, moisture-induced structural weakening, and surface-deterioration-induced crack propagation, respectively. The corresponding initial edge weights are calculated using Eqs. (2)–(9). To reduce the influence of measurement noise, a microscopic edge is retained only when its normalized physical association intensity is greater than ($\varepsilon_{micro} = 0.05$). Self-loops are added to all microscopic nodes during message passing.

For the macroscopic graph, candidate edges between pavement-section supernodes are determined by spatial proximity, traffic-flow correlation, and structural continuity. A directed macroscopic edge ($s_i \to s_j$) is constructed when at least one of the following conditions is satisfied: the center-to-center distance satisfies ($d_{ij} \leq 1000$) m, the Pearson correlation coefficient of traffic flow satisfies ($\rho_{ij} \geq 0.60$), or the two sections have the same pavement structure and moisture-condition category. The integrated macroscopic edge weight is calculated according to Eq. (10), where the weights of spatial distance, traffic-flow correlation, and structural continuity are set to 0.4, 0.4, and 0.2, respectively. The final macroscopic edge is retained only when the normalized integrated edge weight is greater than ($\varepsilon_{\mathrm{macro}} = 0.05$).

All node features, physical boundary variables, and raw edge weights are normalized using min–max statistics calculated from the training set. The physical association intensities are further mapped into the interval (0, 1) using a sigmoid function. Before graph message passing, the weighted adjacency matrix is normalized using the symmetric normalization strategy in Eq. (21). This procedure prevents nodes or sections with large physical weights from dominating the aggregation process and improves the numerical stability of DLPC-GNN training.

2.3 Physics-Based Models for Pavement Distress Evolution Embedded with Mechanical Mechanisms

To overcome the limited generalization capability of deep-learning-based "black-box" models in engineering applications, this study selects and constructs four physical models used to construct physics-informed information edges in the graph structure. These models determine the semantic type, direction, initial weight, and physical attributes of the edges used in GNN message passing.

2.3.1 Unsaturated Seepage Model

The moisture state inside pavement structures is mostly within the unsaturated range. Compared with Darcy's law, the Richards equation can more accurately describe the unsaturated infiltration process of rainfall along microcracks and the capillary rise phenomenon. This equation provides the hydrodynamic basis for hydro-mechanical coupling:

$$\frac{\partial\theta}{\partial t} = \frac{\partial}{\partial z}\left[K(\theta)\left(\frac{\partial\psi}{\partial z} + 1\right)\right] \tag{11}$$

where θ denotes the volumetric water content, $K(\theta)$ is the unsaturated hydraulic conductivity, and ψ represents the matric suction characterizing pore suction in the material. The upper boundary of the model is controlled by the rainfall flux $q_{\text{rain}}(t)$, while the lower boundary is determined by the groundwater table position.

2.3.2 Hydrodynamic Pressure Model

When tires roll over water-rich pavement at high speed, pore water cannot be discharged instantaneously. The intense variation in vertical stress, $\partial\sigma_{zz}(z,t)/\partial t$, may be converted into extremely high transient pore hydrodynamic pressure. This high-frequency scouring action is a direct cause of asphalt stripping and base-course loosening. In this study, the following model is adopted to quantify the hydro-mechanical damage force:

$$p_{\text{hydro}(\text{z,t})} = \frac{\partial\sigma_{zz(z,t)}}{\partial t} \cdot t_{\text{drain}} \tag{12}$$

where t_{drain} denotes the effective drainage time of the structural layer, which is closely related to the material porosity n and hydraulic conductivity K_{hyd}.

2.3.3 Fatigue Crack Propagation Model

For crack evolution within asphalt layers, purely empirical statistical models often exhibit limited transferability across loading and environmental conditions. Therefore, this study introduces the classical Paris law from linear elastic fracture mechanics to describe the fatigue damage accumulation process under an alternating stress field:

$$\frac{da}{dN} = A \cdot (\Delta K)^n \tag{13}$$

where ΔK captures the amplitude of the stress intensity factor at the crack tip and reflects the coupled effect of external loading and crack geometry.

For implementation and subsequent coupling with damage and temperature–aging corrections, Eq. (13) is written in the following parameterized form:

$$\frac{da}{dN} = C_0\,(\Delta\mathrm{K})^m \tag{14}$$

where a is the crack length, N is the number of load cycles, C_0 and m are material-related fatigue parameters, and ΔK denotes the amplitude of the stress intensity factor at the crack tip.

Considering that asphalt pavement cracking is affected not only by cyclic loading but also by accumulated structural damage, pavement temperature, and asphalt aging, the classical Paris law is further modified by introducing a damage correction factor and a temperature–aging coupling correction term:

$$\left(\frac{da}{dN}\right)_{\text{corr}} = C_0 \left(\Delta \mathrm{K}\right)^m \cdot \Phi_D(D_t) \cdot \Phi_{\mathrm{TA}}(T_t, A_t) \tag{15}$$

where $\Phi_D(D_t)$ represents the damage correction factor and $\Phi_{\mathrm{TA}}(T_t, A_t)$ represents the temperature–aging coupling correction term. The damage correction factor is defined as:

$$\Phi_D(D_\mathrm{t}) = 1 + \eta_D D_\mathrm{t} \tag{16}$$

where $D_t \in [0, 1]$ denotes the normalized structural damage index at time step t, and η_D is a non-negative calibration coefficient. In this study, D_t is obtained from the normalized combination of crack area ratio, void-area ratio, and deflection deterioration ratio, which respectively reflect visible crack development, internal structural looseness, and bearing-capacity degradation.

The temperature–aging coupling correction term is expressed as:

$$\Phi_{\mathrm{TA}}(T_\mathrm{t}, A_\mathrm{t}) = \exp(\eta_T \tilde{T}_\mathrm{t} + \eta_A A_\mathrm{t} + \eta_{TA} \tilde{T}_\mathrm{t} A_\mathrm{t}) \tag{17}$$

where $\tilde{T}_t$ is the normalized pavement temperature deviation from the reference temperature, $A_t \in [0, 1]$ is the normalized asphalt aging index, and η_T, η_A, and η_{TA} are calibration coefficients. The aging index is calculated from aging-sensitive material indicators, such as penetration reduction, ductility reduction, and softening-point increase. The interaction term $\tilde{T}_t A_t$ is introduced because aged asphalt materials generally exhibit higher cracking susceptibility under unfavorable temperature conditions.

The corrected fatigue crack-growth rate $(da/dN)_{\text{corr}}$ is not directly used as an additional independent input feature. Instead, it is normalized and used to modulate the attention coefficient of the fatigue feedback edge from the surface-deterioration node to the cracking-related node in the microscopic distress graph; the initial edge weight of this path remains defined by the texture-depth loss ratio in Eq. (9). In this way, the modified Paris law provides a physically interpretable prior for the feedback path by which surface deterioration and material degradation accelerate crack propagation.

2.3.4 Bounded Deflection Evolution Model

Surface deflection is a key indicator for evaluating the overall stiffness of pavement structures. As the service period increases, the deflection value gradually rises. However, from the perspective of physical rationality, even when the pavement structure is completely damaged, the underlying subgrade still retains residual bearing capacity; therefore, deflection cannot approach infinity. To prevent purely neural-network-based long-term prediction from producing physically unrealistic numerical divergence, this study proposes an asymptotically bounded deflection evolution equation:

$$D(t) = D_0 + (D_{\max} - D_0) \cdot \left[1 - \exp\left(-\alpha \int_0^t N(\tau) \cdot d(\tau)\, d\tau\right)\right] \tag{18}$$

This model strictly constrains the physical boundary of the prediction results through the initial deflection D_0 and the ultimate failure deflection $D_{\max}$, while the integral term represents the fatigue effect induced by cumulative traffic loading. The mapping between the four physical laws and the corresponding information edges is summarized in Table 1.

Table 1: Mapping between physical laws and physics-informed information edges in DLPC-GNN.

Physical Model	Corresponding Information Edge	Edge Direction	Physical Meaning	Role in GNN
Richards equation	Infiltration edge	Crack → structural water damage	Crack-induced rainfall infiltration	Defines edge existence and initial weight
Hydrodynamic pressure model	Scouring edge	Structural water damage → surface damage	Pore-water pressure and base-course loosening	Provides edge attribute for message passing
Paris law	Fatigue feedback edge	Surface damage → crack	Stress concentration accelerates crack propagation	Modulates attention coefficient
Bounded deflection model	Bearing-capacity degradation edge	Segment-level supernode → segment-level supernode	Physically bounded structural deterioration	Constrains macro-scale propagation edge

2.3.5 Multi-Scale Temporal Aggregation of Physical Mechanisms

The physical mechanisms incorporated in DLPC-GNN are characterized by distinctly different time scales. Rainfall-induced seepage generally evolves over minutes to hours, wheel-load-induced hydrodynamic pressure varies over seconds or sub-seconds, whereas fatigue crack growth and deflection degradation are long-term cumulative processes occurring over months to years. Therefore, the graph snapshot used in this study should not be interpreted as an instantaneous physical field in which all governing processes are solved at the same temporal resolution. Instead, each graph snapshot represents the equivalent pavement state and the aggregated physical driving factors within a unified maintenance-oriented observation window.

In the present implementation, the graph-sequence time step is defined according to the pavement inspection and maintenance evaluation cycle. Fast processes are converted into window-level statistical or cumulative descriptors before graph construction. Specifically, rainfall infiltration is represented by aggregated hydrological boundary variables, including cumulative rainfall, maximum rainfall intensity, antecedent rainfall index (a decay-weighted sum of rainfall over preceding observation windows), effective infiltration flux, and equivalent hydraulic head difference. The transient hydrodynamic pressure induced by wheel loading is represented by event-level descriptors, such as peak value, upper-percentile value, duration above a predefined threshold, and cumulative hydrodynamic pressure impulse within the observation window. These descriptors do not imply that the transient response is directly averaged as a slow deterioration variable; rather, they quantify the intensity of repeated short-duration hydraulic impacts acting on the pavement structure during the observation period.

By contrast, fatigue crack propagation and bounded deflection degradation are treated as slow state-evolution variables. Their values are updated between consecutive graph snapshots according to accumulated traffic loading, material aging, moisture condition, and previous distress states. Under this formulation, fast hydro-mechanical processes act as intra-window driving factors, whereas fatigue cracking and deflection degradation represent inter-window accumulated deterioration states. This separation enables multi-scale physical processes to be fused within a unified graph-learning framework without assuming that all mechanisms share the same intrinsic time scale.

3 Dual-Layer Progressive Physics-Constrained Graph Neural Network

To effectively characterize the multi-scale spatial evolution of asphalt pavement structural distresses and achieve deep integration between physical mechanisms and data-driven learning, this study develops a Dual-Layer Progressive Physics-Constrained Graph Neural Network (DLPC-GNN). The proposed network adopts graph structures as a unified representation framework. At the microscopic level, a multi-head graph attention network is employed to adaptively model the nonlinear physical associations among typical distress nodes, including cracks, surface deterioration, and structural moisture-induced damage, thereby enabling efficient aggregation and propagation of multi-source features. At the macroscopic level, an attention pooling mechanism is used to map the high-order features learned from the microscopic layer onto pavement-section-level supernodes, thereby constructing a high-level graph representation that reflects the spatial topological relationships of the road network.

Meanwhile, to overcome the limitations of conventional purely data-driven methods in terms of physical consistency and interpretability, multi-source physical constraints are introduced during network training. Specifically, a joint loss function integrating mechanical response constraints, material boundary constraints, and distress evolution logic constraints is constructed to impose physical feasibility constraints on the model parameter space. On this basis, a progressive training strategy is further designed, in which physical constraints are introduced gradually to alleviate the non-convexity of the optimization process. As a result, the proposed model can significantly improve physical consistency and generalization capability while maintaining high prediction accuracy. The overall architecture of the Dual-Layer Progressive Physics-Constrained Graph Neural Network is illustrated in Fig. 3.

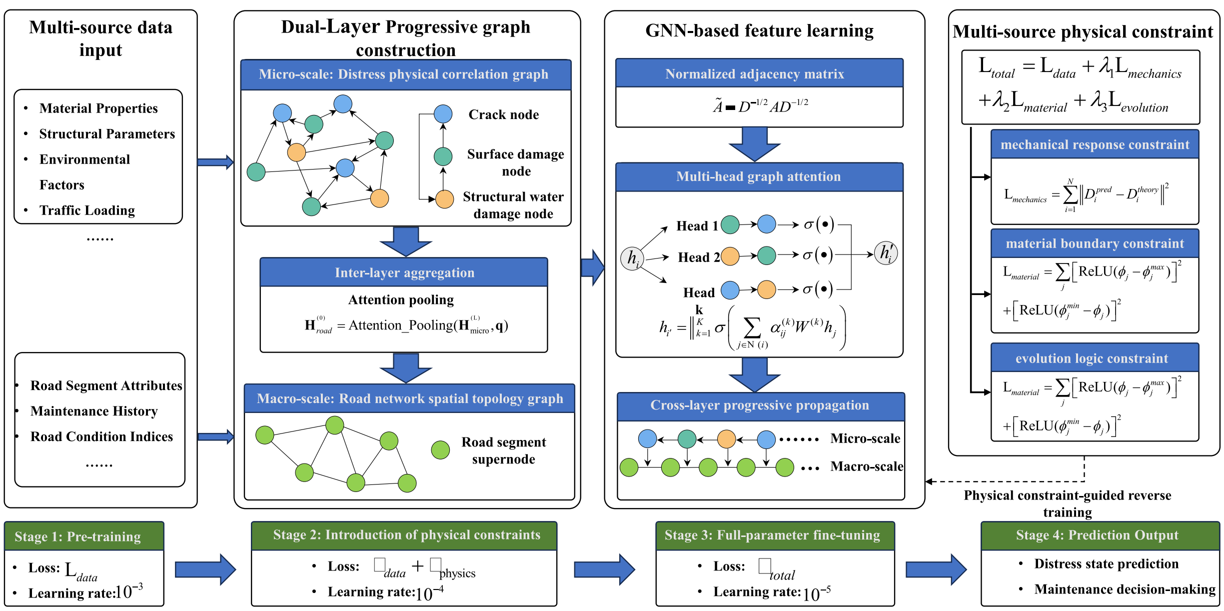

Figure 3: Dual-Layer progressive physics-constrained graph neural network framework.

3.1 GNN Architecture

3.1.1 Multi-Head Graph Attention Network

A multi-head graph attention network is adopted to implement message passing in the microscopic layer:

$$h_{i'} = \|_{k=1}^{K} \sigma\left(\sum_{j\in\mathcal{N}(i)} \alpha_{ij}^{(k)} W^{(k)} h_j\right) \tag{19}$$

where K denotes the number of attention heads, $\|$ represents the concatenation operation, and $\alpha_{ij}^{(k)}$ is the attention coefficient of the k-th head. The attention coefficient is calculated as:

$$\alpha_{ij} = \frac{\exp\left(\text{LeakyReLU}\left(\mathbf{a}^T\left[Wh_i \| Wh_j\right]\right)\right)}{\sum_{k\in\mathcal{N}(i)} \exp\left(\text{LeakyReLU}\left(\mathbf{a}^T\left[Wh_i \| Wh_k\right]\right)\right)} \tag{20}$$

3.1.2 Normalized Adjacency Matrix

A symmetric normalization strategy is adopted for the adjacency matrix:

$$\tilde{A} = D^{-1/2} A D^{-1/2} \tag{21}$$

where D is the degree matrix, with $D_{ii} = \sum_j A_{ij}$.

3.1.3 Inter-Layer Aggregation

The output of the microscopic layer is aggregated into pavement-section-level supernodes through attention pooling:

$$\boldsymbol{H}_{\text{road}}^{(0)} = \text{Attention\_Pooling}(\boldsymbol{H}_{\text{micro}}^{(L)}, \boldsymbol{q}) \tag{22}$$

where $H_{\text{micro}}^{(L)}$ denotes the high-level node representation output by the L-th microscopic graph layer, and q is the learnable query vector used in the attention pooling operation.

3.2 Construction of the Multi-Source Physics-Constrained Joint Loss Function

In addition to the edge-level physical embedding described above, a lightweight auxiliary physics-constrained loss is further introduced to prevent the learned edge weights and predicted states from deviating from physically reasonable ranges, this study constructs a multi-source joint loss function $\mathcal{L}_{total}$, consisting of a data-driven term and multiple physics-constrained terms:

$$L_{\text{total}} = L_{\text{data}} + \lambda_1 L_{\text{mechanics}} + \lambda_2 L_{\text{material}} + \lambda_3 L_{\text{evolution}} \tag{23}$$

where L_{data} denotes the supervised data-fitting loss, while $L_{\text{mechanics}}$, L_{material}, and $L_{\text{evolution}}$ represent the mechanical response constraint, material boundary constraint, and distress evolution logic constraint, respectively. The coefficients λ_1, λ_2, and λ_3 are weighting parameters used to balance different loss components. To ensure that the predicted deflection values have clear structural-mechanical significance, the network output D_i^{pred} is forced to approach the theoretical solution D_i^{theory} derived from elastic layered system theory. This theoretical solution computes the surface deflection of a multilayer elastic system from its material and structural parameters. Accordingly, the mechanical response constraint is defined as:

$$L_{\text{mechanics}} = \sum_{i=1}^{N} \left\| \mathrm{D}_i^{\text{pred}} - \mathrm{D}_i^{\text{theory}} \right\|^2 \tag{24}$$

where the theoretical deflection is calculated using the multilayer system integral formulation:

$$D_{\text{theory}} = \frac{2(1-\nu^2)}{E} \int_0^\infty \frac{J_1(\mathrm{mr}) \cdot J_1(\mathrm{ma})}{m \cdot f(m, \boldsymbol{E}, \boldsymbol{h}, \boldsymbol{\nu})} \mathrm{dm} \tag{25}$$

In this equation, E and ν denote the elastic modulus and Poisson's ratio, respectively; $J_1(\cdot)$ is the first-order Bessel function; h denotes the layer thickness; and $f(m, \mathbf{E}, \mathbf{h}, \boldsymbol{\nu})$ represents the mechanical transfer function of the multilayer pavement system. The physical parameters of asphalt layers and semi-rigid base layers, such as modulus and Poisson's ratio, have explicit engineering ranges. Therefore, a material boundary penalty is constructed using the rectified linear unit (ReLU) activation function, which forces the implicitly extracted physical feature ϕ_j to remain within its reasonable lower and upper bounds $\left[\phi_j^{\min}, \phi_j^{\max}\right]$ during backpropagation. The material boundary constraint is given by:

$$L_{\text{material}} = \sum_j \left[\mathrm{ReLU}(\phi_j - \phi_j^{\max})\right]^2 + \left[\mathrm{ReLU}(\phi_j^{\min} - \phi_j)\right]^2 \tag{26}$$

To ensure that the adaptively learned adjacency weights W_{learned} do not significantly deviate from the physics-based theoretical evolution weights W_{physics}, an evolution logic constraint is further introduced. This constraint guarantees the interpretability of the prediction results at the underlying graph-evolution level:

$$L_{\text{evolution}} = \left\| W_{\text{learned}} - W_{\text{physics}} \right\|_{\mathrm{F}}^2 \tag{27}$$

where $\|\cdot\|_{\mathrm{F}}$ denotes the Frobenius norm. By constraining the learned graph topology with physically defined evolution weights, the model is encouraged to preserve the intrinsic deterioration logic among pavement distresses during representation learning.

3.3 Progressive Training Strategy

The introduction of physical constraint terms substantially increases the non-convexity of the loss landscape. Direct end-to-end training may therefore cause the optimization process to become trapped in local minima. To address this issue, this study designs a three-stage progressive optimization strategy, consisting of data warm-up, physical-rule introduction, and full-parameter fine-tuning. This strategy balances data feature extraction and physical-law fitting during model training. The detailed configuration of the three-stage progressive training strategy is summarized in Table 2.

Table 2: Progressive training strategy.

Stage	Loss Function	Learning Rate	Training Epochs
Stage 1: Pre-training	L_{data}	$\eta = 10^{-3}$	50 epochs
Stage 2: Physics-constrained training	$L_{\text{data}} + 0.1L_{\text{physics}}$	$\eta = 10^{-4}$	30 epochs
Stage 3: Fine-tuning	L_{total}	$\eta = 10^{-5}$	20 epochs

In the first stage, only the data-driven loss L_{data} is used to enable the network to learn the fundamental nonlinear mapping relationship from multi-source inspection data. In the second stage, the physical constraint term is introduced with a relatively small weight, allowing the model to gradually adapt to the physical prior information while avoiding abrupt changes in the optimization direction. In the third stage, the complete joint loss function L_{total} is adopted for full-parameter fine-tuning, so that the model can simultaneously satisfy data-fitting accuracy, mechanical response rationality, material boundary feasibility, and distress evolution consistency. This progressive training scheme improves convergence stability and enhances the engineering reliability of the DLPC-GNN model.

3.4 Practical Implementation of DLPC-GNN

To further clarify the technical realization of the proposed framework, this subsection describes how DLPC-GNN is implemented from raw inspection records to model prediction. In the practical implementation, multi-source pavement inspection data are first collected from automated pavement detection, ground-penetrating radar, falling weight deflectometer, traffic monitoring, material testing, and environmental monitoring systems. These data include pavement surface morphology, structural response, layer thickness, material parameters, traffic loading, rainfall intensity, and moisture-related boundary conditions. Since different inspection devices usually have different sampling intervals and spatial resolutions, all raw records are first matched to the corresponding pavement monitoring section and then synchronized according to their timestamps. To further handle the temporal-scale mismatch among different physical mechanisms, a temporal aggregation strategy is adopted before constructing graph-sequence samples. The raw high-frequency or event-based variables are first mapped into the same observation window as the graph snapshot. For hydrological variables, cumulative rainfall, maximum rainfall intensity, rainfall duration, antecedent rainfall index, and equivalent hydraulic head difference are calculated. For traffic-induced hydrodynamic pressure, the peak value, upper-percentile value, threshold-exceedance duration, and cumulative pressure impulse are extracted to characterize the repeated transient scouring effect within the window. For slow deterioration variables, such as crack area, crack length, material aging indicators, and deflection response, the latest inspection value or temporally interpolated value is used as the state variable of the corresponding graph snapshot. Therefore, the graph input at each time step consists of both slow pavement-state variables and aggregated fast-process driving variables. Variables with inconsistent sampling intervals are aligned to the same observation time step using interpolation, while abnormal records and missing values are processed before feature normalization.

After data preprocessing, the investigated expressway section is discretized into pavement monitoring sections. Each section in one travel direction is represented as a macroscopic pavement-section supernode. Within each supernode, three microscopic distress nodes are further constructed to describe cracking-related distress, surface deterioration, and structural moisture-induced damage, respectively. The feature vector of each microscopic node is assembled from the corresponding inspection variables defined in Section 4.2.1. In this way, the heterogeneous inspection records are transformed into structured node features with clear engineering meanings.

Based on the constructed nodes, the dual-layer graph topology is then established. At the microscopic level, directed physical association edges are built among the three distress nodes to represent crack-induced moisture infiltration, moisture-induced structural weakening, and surface-deterioration-induced crack propagation. The initial weights of these edges are calculated using the physics-informed formulations in Eqs. (2)–(9). At the macroscopic level, pavement-section supernodes are connected according to spatial distance, traffic-flow correlation, and structural continuity, so that the regional propagation tendency of pavement deterioration can be represented. All raw edge weights are normalized using the statistics of the training set and are further processed by the adjacency normalization strategy in Eq. (21) before graph message passing.

The normalized node feature tensors, microscopic and macroscopic adjacency matrices, physical boundary-condition tensors, and maintenance strategy labels are finally organized as spatiotemporal graph-sequence samples. During model training, these samples are fed into DLPC-GNN following the progressive training strategy described in Section 3.3. The network is first optimized using the data-driven loss to learn the basic nonlinear mapping relationship, then gradually constrained by the physics-informed loss terms, and finally fine-tuned using the complete joint loss function. During inference, the trained model receives the latest graph-sequence sample as input and outputs the predicted pavement distress state together with the corresponding maintenance strategy category. Therefore, the proposed framework forms a complete computational procedure that links multi-source data processing, graph construction, physics-informed message passing, model optimization, and maintenance-oriented prediction.

4 Experiments

4.1 Project Overview

The Huizhou section of the Huizhou–Shenzhen Expressway, including K0 + 000–K7 + 950 and K3595 + 164–K3619 + 405, has a total length of 32.191 km. The section starts from Gutang'ao in Huizhou City and ends at Kengtangjing. The mainline is a two-way eight-lane expressway, with a standard subgrade width of 41 m. The design speed is 100 km/h, while the operating speed is 120 km/h. The lane configuration is shown in Fig. 4.

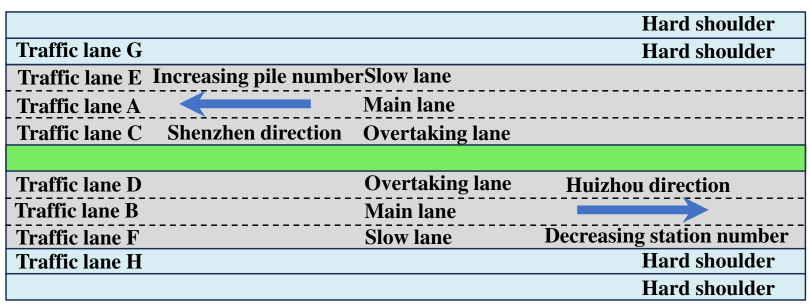

Figure 4: The lane configuration.

The standard cross-section of the asphalt pavement subgrade is configured as follows. The integral subgrade has a width of 33.5 m, including a 2.0 m central median, two 0.75 m marginal strips, six 3.75 m traffic lanes, two 3.0 m hard shoulders, and two 0.75 m earth shoulders. The pavement structure varies according to the moisture condition of the road section, as summarized in Table 3.

A modified emulsified asphalt tack coat is applied between asphalt layers. A diluted asphalt prime coat and a hot asphalt lower seal coat are applied on the top surface of the base layer. The hard shoulder adopts the same pavement structure and thickness as the corresponding carriageway, while the earth shoulder is vegetated.

Table 3: The pavement structure.

Layer	Material	Dry Section	Med.-Moist. Section
Surface layer	GAC-16C medium-grained modified asphalt concrete	5 cm	5 cm
Intermediate layer	GAC-20C medium-grained modified asphalt concrete	6 cm	6 cm
Lower layer	GAC-25C coarse-grained asphalt concrete	8 cm	8 cm
Upper base	Cement-stabilized graded crushed stone	18 cm	18 cm
Lower base	Cement-stabilized graded crushed stone	18 cm	18 cm
Subbase	Low-dose cement-stabilized graded crushed stone	20 cm	20 cm
Cushion layer	Unscreened crushed stone	/	20 cm
Total thickness	—	75 cm	95 cm

4.2 Dataset Construction

To effectively support the training of the DLPC-GNN and validate its physical consistency, this study constructs a multimodal integrated dataset based on structural health monitoring and nondestructive testing techniques. The dataset covers material-level microscopic properties, macroscopic service conditions, and environmental boundary conditions. The data organization and acquisition methods strictly follow pavement engineering evaluation specifications and mechanical testing standards, ensuring that the boundary conditions of the partial differential equations embedded in the physics-informed neural network are physically realistic and engineering-representative.

4.2.1 Graph Topology and Multi-Source Tensor Data Structure for DLPC-GNN

Considering that asphalt pavement structural deterioration is a typical nonlinear spatiotemporal evolution process, the conventional tabular inspection records are reconstructed into a high-dimensional spatiotemporal graph sequence for DLPC-GNN. In the engineering implementation, the investigated 32.191-km expressway section is discretized according to physical monitoring sections rather than fixed image grids. Each macroscopic pavement-section supernode corresponds to a road segment of approximately 500 m in length, covering all lanes in one traffic direction. Considering the two travel directions, the macroscopic graph contains 130 pavement-section supernodes at each observation time step.

For each macroscopic supernode, three microscopic distress nodes are defined, corresponding to cracking-related distress, surface deterioration, and structural moisture-induced damage. Therefore, each dual-layer graph snapshot contains 130 macroscopic supernodes and 390 microscopic distress nodes. Based on the synchronized multi-source inspection records, including pavement surface morphology, structural response, material parameters, traffic loading, and environmental boundary conditions, a total of 15,400 spatiotemporal graph snapshots are generated for model training and testing. This engineering implementation ensures that the proposed graph structure corresponds to real physical monitoring sections and measurable pavement distress variables, rather than being a conceptual or artificially defined topology.

(1) Heterogeneous node feature tensor

At the microscopic layer, specific pavement distresses are treated as graph nodes. Mechanical and physical representations with different dimensions are extracted and decoupled into three feature subtensors. At the microscopic layer, three types of distress nodes are defined within each macroscopic pavement-section supernode, namely cracking-related type-A nodes, surface-deterioration type-B nodes, and structural moisture-induced damage type-C nodes. For the (i)-th pavement section at time step (t), the initial feature vector of the type-A node is defined as ($x_{\mathrm{A}}^{i,t} \in \mathrm{R}^7$), including crack area ($\mathrm{A_{crack}}$), crack length ($\mathrm{L_{crack}}$), average crack width (w_{crack}), softening point (SP), ductility (DU), penetration (PEN), and aggregate gradation index (G). These variables are obtained from automated pavement detection images, line-laser profiles, periodic core sampling, laboratory material tests, and construction records, and are used to characterize crack development, asphalt aging, and fracture resistance. The initial feature vector of the type-B node is defined as ($x_{\mathrm{B}}^{i,t} \in \mathrm{R}^5$), including texture depth (TD), friction coefficient (FR), international roughness index (IRI), surface-layer thickness ($\mathrm{H_{surf}}$), and intermediate-layer thickness ($\mathrm{H_{inter}}$). These variables are extracted from the automated pavement detection system, Sideway-force Coefficient Routine Investigation Machine (SCRIM), 3D-GPR, and pavement structure records, and are used to describe surface service condition and geometric deterioration. The initial feature vector of the type-C node is defined as ($x_{\mathrm{C}}^{i,t} \in \mathrm{R}^6$), consisting of equivalent permeability coefficient ($\mathrm{K_{perm}}$), moisture content (θ), equivalent internal water head (h_{b}), central deflection (d_0), back-calculated dynamic modulus ($\mathrm{E_{dyn}}$), and void-area ratio (r_{void}). These variables are obtained from permeability tests, time-domain reflectometry (TDR) sensors, groundwater-level monitoring, falling weight deflectometer (FWD) tests, 3D-GPR, and CT-assisted void inversion, and are used to represent internal moisture condition, void development, and structural bearing-capacity degradation. Before being fed into the microscopic graph neural network, all node features are normalized using the training-set statistics and then projected into the same hidden dimension through type-specific linear embedding layers to ensure dimensional consistency during graph message passing.

(2) Physics-driven dynamic adjacency matrices

Unlike conventional graph networks that adopt binarized adjacency matrices or distance-based edge weights, the proposed dataset records intermediate mechanical parameters used to initialize physics-based evolution edges.

The microscopic physical association matrix is defined as:

$$\boldsymbol{A}_{\mathrm{micro}}^{t} \in R^{(\mathrm{N_A}+\mathrm{N_B}+\mathrm{N_C})\times(\mathrm{N_A}+\mathrm{N_B}+\mathrm{N_C})} \tag{28}$$

This matrix stores asymmetric directed edge weights calculated from hydro-mechanical coupling theory. Representative parameters include crack area A_{crack}, hydraulic head difference Δh, and seepage path length L_{path}, which are used to calculate rainfall infiltration effects. It also includes the tensile stress at the bottom of structural layers $\sigma_{\mathrm{tensile}}$ and the internal void-area ratio $A_{\mathrm{void}}/A_{\mathrm{total}}$, which are used to quantify structural bearing-capacity deterioration.

The macroscopic spatial topology matrix is defined as:

$$\boldsymbol{A}_{\mathrm{macro}}^{t} \in R^{M\times M} \tag{29}$$

This matrix integrates spatial feature tensors, including the inter-section distance d_{ij}, traffic-flow correlation intensity T_{ij}, and structural continuity indicator S_{ij}.

To calculate the mechanical and evolution constraints in the loss function, a physical boundary condition tensor is further constructed:

$$\boldsymbol{P}_{\mathrm{bound}}^{t} \in R^{M\times C_{\mathrm{phys}}} \tag{30}$$

where C_{phys} denotes the dimension of the physical parameters. This tensor contains the number of load cycles N_{cycles}, rainfall intensity q_{rain}, groundwater level z_{GW}, drainage time t_{drain}, dynamic modulus E of each structural layer, and Poisson's ratio v. These parameters are dynamically fed into the Richards unsaturated seepage equation and the Paris fatigue crack propagation model during training.

(3) Maintenance decision label matrix

The maintenance decision labels are encoded as a one-hot tensor:

$$\boldsymbol{Y}_{\text{maint}} \in R^{M \times K} \tag{31}$$

where K denotes the total number of discrete maintenance strategy categories, including preventive maintenance, corrective maintenance, and structural rehabilitation.

The microscopic physical association matrix and the macroscopic spatial topology matrix are constructed according to the graph-construction protocol in Section 2.2.3 and used as direct graph inputs after adjacency normalization. The detailed feature-alignment and normalization procedures are provided in Section 4.2.3.

4.2.2 Multi-Source Data Acquisition

To ensure the engineering authenticity and mechanical fidelity of the graph-network input data, this study establishes a multi-source data acquisition system. All features and physical boundary parameters are collected using high-precision equipment.

(1) Pavement surface geometry and morphology acquisition.

Macroscopic surface features are obtained using an automated pavement detection vehicle (APD). The system integrates a three-dimensional line laser profiler and a high-frequency line-scan camera, enabling real-time extraction of crack geometric area A_{crack}, texture depth loss ratio TD_{loss}, and IRI at millimeter-level resolution under normal traffic speed. The surface friction coefficient FR is continuously measured using a Sideway-force Coefficient Routine Investigation Machine (SCRIM).

(2) Internal mechanical response and structural damage detection.

Three-dimensional ground-penetrating radar (3D-GPR) is used for continuous nondestructive scanning. By analyzing the differences in reflected dielectric constants and attenuation characteristics of high-frequency electromagnetic waves at the interfaces of different structural layers, the layer thicknesses $\left(H_{\text{top}}, H_{\text{mid}}\right)$ are accurately extracted. The evolution of microvoids and the void area A_{void} inside the base layer are also quantitatively inverted.

A falling weight deflectometer (FWD) is used for fixed-point impulse-loading tests to measure the current central deflection value D_{defl}, which characterizes the current overall structural stiffness. The model parameters $D_0, D_{\max}$ are not directly measured by the current FWD test: D_0 is obtained from construction-stage or earliest available baseline records, and Dmax is calibrated from historical failure-state data or engineering limits. Meanwhile, the back-calculated dynamic modulus E_{modulus} of each structural layer is extracted using back-calculation software and used as an input prior for calculating the theoretical mechanical loss $L_{\text{mechanics}}$.

(3) Acquisition of material rheological and hydrological prior parameters.

Basic material indicators such as softening point T_{soft} and penetration P_{penet} are obtained not only from historical construction records but also from periodic core sampling in the test sections. The core samples are sent to the laboratory for verification using standard Marshall tests and dynamic modulus tests.

For permeability coefficient K_{perm} and porosity n, which characterize water migration behavior, accurate measurements are obtained by combining constant-head or falling-head permeability tests with industrial computed tomography scanning. The groundwater level z_{GW} and subgrade moisture content are monitored in real time using time-domain reflectometry sensors embedded in the subgrade.

(4) Dynamic monitoring of external traffic loading and environmental boundary conditions.

Road-network-level traffic-flow correlation features T_{ij} and cumulative equivalent standard axle load repetitions N_{cycles} are recorded in real time using weigh-in-motion systems installed at key cross-sections. Meteorological rainfall intensity q_{rain} is directly collected from microwave weather radar and micro-weather stations along the road section and converted to an effective infiltration flux, which serves as the upper flux boundary condition of the Richards equation after runoff and infiltration losses are considered.

4.2.3 Conversion from Raw Inspection Data to Model Input Features

To make the conversion from raw inspection records to DLPC-GNN input features more transparent, the feature extraction, heterogeneous data alignment, and normalization procedures are further described in this subsection. All raw data were first referenced to the same pavement monitoring section according to the route stake number, travel direction, lane information, and inspection mileage. The 32.191-km expressway section was divided into physical monitoring sections of approximately 500 m in length, and all inspection records falling within the same section were assigned to the corresponding macroscopic pavement-section supernode. The microscopic distress features within each supernode were then organized according to the three distress-node types defined in Section 4.2.1.

The correspondence between inspection sources and extracted variables is summarized in Table 4. The automated pavement detection system provides surface morphology indicators, including crack geometric area, crack length and width, texture depth, international roughness index, and surface distress morphology. The 3D-GPR data are used to extract layer thickness, abnormal dielectric response, base-course void indicators, and moisture-sensitive zones. FWD testing provides current central deflection, deflection-basin characteristics, and back-calculated dynamic modulus; D0 is derived from construction-stage or earliest available baseline records, and Dmax is calibrated from historical failure-state data or engineering limits. Weigh-in-motion (WIM) records are used to derive traffic loading variables, including traffic volume, axle load spectrum, cumulative equivalent standard axle load repetitions, and traffic-flow correlation among pavement sections. Time-domain reflectometry (TDR) sensors provide subgrade moisture content and moisture-state variation, while weather radar and micro-weather stations provide rainfall intensity, cumulative rainfall, and rainfall duration. Material-related indicators, including penetration, ductility, softening point, permeability coefficient, porosity, and aggregate gradation, are obtained from historical construction records and periodic core sampling tests.

After feature extraction, the heterogeneous records were aligned in both space and time. Spatial alignment was performed by mapping all raw inspection records to the nearest pavement monitoring section using mileage coordinates and travel direction. When several records were located within the same section and observation period, statistical aggregation was applied according to the physical meaning of the variable. For example, the mean value was used for continuously distributed indicators such as IRI, texture depth, deflection, and moisture content; the maximum or upper-percentile value was used for safety-critical distress indicators such as crack area, void indicator, and hydrodynamic-pressure-related variables; and the cumulative value was used for traffic load repetitions and rainfall-related variables.

Table 4: Correspondence between raw inspection sources and extracted model variables.

Data Source	Raw Inspection Records	Extracted Variables	Role in DLPC-GNN Input
APD/automated pavement detection	Line-scan images, 3D laser profiles, surface distress records	Crack area, crack length, crack width, texture depth, IRI, surface distress morphology	Cracking-related and surface-deterioration node features; crack-induced moisture-damage edge initialization
3D-GPR	Radar profiles, dielectric response, layer-interface reflections	Layer thickness, dielectric anomaly, base-course void indicator, moisture-sensitive zone	Structural moisture-induced damage node features; seepage path and void-related edge variables
FWD	Deflection basin under impulse loading	Current central deflection, deflection-basin parameters, and back-calculated layer modulus	Moisture-induced damage node features; mechanical response constraint; bounded deflection model
WIM	Axle load, vehicle count, traffic flow records	Axle load spectrum, cumulative equivalent standard axle load repetitions, traffic-flow correlation	Macroscopic topology edge construction; traffic-loading boundary condition
TDR	Subgrade moisture and local water-content monitoring	Moisture content, moisture-state variation, equivalent internal water head	Hydrological boundary tensor; unsaturated seepage-related edge initialization
Weather radar/micro-weather station	Rainfall intensity, rainfall duration, cumulative rainfall	Rainfall intensity, rainfall flux, cumulative rainfall, antecedent rainfall index	Rainfall boundary condition; crack-induced infiltration edge initialization
Material tests and construction records	Core sampling, laboratory tests, design documents	Penetration, ductility, softening point, permeability coefficient, porosity, aggregate gradation	Material-related node features; material boundary constraint; aging-related fatigue correction

Temporal alignment was performed using a unified observation time step. Continuous monitoring data, such as WIM, TDR, and meteorological records, were aggregated within the corresponding observation window. Periodic inspection data, such as APD, 3D-GPR, and FWD records, were assigned to the closest observation time according to the inspection timestamp. When the sampling intervals of different sources were inconsistent, spline interpolation was used for smoothly varying variables such as moisture content and temperature-related indicators, while stepwise holding was used for relatively stable material and structural parameters such as layer thickness, permeability coefficient, aggregate gradation, and laboratory-measured asphalt properties. Missing values caused by temporary sensor interruption or incomplete inspection coverage were processed using section-neighbor interpolation and temporal interpolation when the missing duration was short. Samples with physically abnormal values outside the allowable engineering range were removed or clipped before normalization.

The aligned variables were then converted into four types of model inputs: node feature tensors, physics-driven adjacency matrices, physical boundary-condition tensors, and maintenance strategy labels. The node feature tensors describe the local state of cracking-related distress, surface deterioration, and structural moisture-induced damage. The physics-driven adjacency matrices store the normalized edge weights calculated from crack-induced infiltration, moisture-induced weakening, fatigue feedback, and macroscopic spatial propagation mechanisms. The physical boundary-condition tensor contains rainfall intensity, groundwater level, moisture state, drainage time, number of load cycles, dynamic modulus, and Poisson's ratio, which are used in the physics-informed edge initialization and physical constraint terms. The maintenance strategy labels are encoded as one-hot vectors corresponding to preventive maintenance, corrective maintenance, and structural rehabilitation.

To avoid information leakage, all normalization parameters were calculated only from the training set and then applied unchanged to the validation and testing sets. For a scalar feature (x), min–max normalization was performed. For variables with strong skewness, such as crack area, void indicator, traffic load repetitions, and rainfall accumulation, logarithmic transformation was first applied before min–max normalization. Raw physical edge weights were normalized using the same training-set statistics and were further mapped into ([0, 1]) by the sigmoid function before adjacency normalization. Through this procedure, multi-source heterogeneous inspection records were converted into consistent spatiotemporal graph-sequence samples for DLPC-GNN training and testing.

4.3 Model Training Settings and Hyperparameter Configuration

To comprehensively evaluate the prediction performance and generalization capability of DLPC-GNN, the constructed dataset containing 15,400 spatiotemporal graph snapshots is divided into training and testing sets at a ratio of 7:3. In addition, 10% of the training set is randomly selected as a validation set for hyperparameter tuning and model selection.

Considering the structural continuity and traffic-flow distribution characteristics in practical pavement engineering, the supernodes in the macroscopic graph are not defined using conventional fixed pixel grids. Instead, each macroscopic supernode is mapped to a physical monitoring section with a length of approximately 500 m and a width covering all lanes in one traffic direction.

Because the model input integrates multi-source heterogeneous parameters, including macroscopic geometry, microscopic mechanics, and hydrodynamic variables, the feature dimensions and numerical scales may differ by several orders of magnitude. To avoid gradient explosion when solving the physical partial differential equation constraints, a min–max normalization strategy is applied before network input, scaling all node features and physical boundary parameters into the range [0, 1].

For backpropagation in the deep neural network, the Adam optimizer is used for gradient updating, with $\beta_1 = 0.9$, $\beta_2 = 0.999$, and $\epsilon = 10^{-7}$. To effectively handle the highly non-convex loss landscape caused by the introduction of physical constraints, the three-stage progressive training strategy described above is strictly implemented. The total number of training epochs is set to 100, and the batch size is set to 16 graph-sequence snapshots.

Stage 1: Data pre-training. During the first 50 epochs, only the data-driven loss L_{data} is optimized. The initial learning rate is set to $lr = 10^{-3}$.

Stage 2: Physical-rule introduction. From epoch 51 to epoch 80, a joint physics-constrained loss with a weight of 10%, namely $0.1L_{physics}$, is introduced. The learning rate is reduced to $lr = 10^{-4}$.

Stage 3: Full-parameter fine-tuning. During the final 20 epochs, the total loss function L_{total} is activated for joint fine-tuning. The learning rate is further reduced to $lr = 10^{-5}$.

In the fine-tuning stage, an exponential learning-rate decay strategy with a decay rate of 0.9 is applied to prevent overfitting under complex physical constraints. An early stopping technique with a patience of 15 epochs is also introduced.

After multiple rounds of grid search and cross-validation on the validation set, the final network hyperparameters of DLPC-GNN are configured as follows. The number of attention heads in the microscopic multi-head graph attention network is set to $K = 8$. The hidden feature dimension of microscopic nodes is set to 128. The dimension of pavement-section supernodes after microscopic-to-macroscopic pooling is set to 256. The number of graph attention message-passing layers is set to 3. The physical constraint weights in the joint loss function are assigned as $\lambda_1 = 0.4$, $\lambda_2 = 0.3$, and $\lambda_3 = 0.3$, ensuring balanced constraint effects among mechanical response, material boundary, and evolution logic during gradient backpropagation.

To further evaluate the computational feasibility of DLPC-GNN, the approximate computational cost of the proposed framework was analyzed during model training and inference. The implementation was conducted on a workstation equipped with an Intel Xeon Gold 6226R CPU, an NVIDIA GeForce RTX 3090 GPU with 24 GB memory, and 128 GB RAM, using PyTorch 2.0.1 with CUDA 11.8. The full dataset contains 15,400 spatiotemporal graph-sequence samples. Under the 7:3 split and the 10% validation holdout described above, 9702 samples are used for parameter optimization, 1078 for validation, and 4620 for testing; the batch size is 16 and the total number of training epochs is 100.

The trainable parameter size of DLPC-GNN is approximately 1.26 million. The average training time per epoch is approximately 19.4 s, and the total training time for 100 epochs is approximately 32.3 min. During inference, the average prediction time for one graph-sequence sample is approximately 2.6 ms, while the average prediction time for one batch is approximately 34.8 ms. The peak GPU memory consumption during training is approximately 4.2 GB.

From the perspective of computational complexity, the main computational cost of DLPC-GNN comes from the multi-head graph attention layers and the physics-constrained loss calculation. For a sparse graph, the computational complexity of each graph attention layer is approximately proportional to the number of nodes and edges, i.e., (O(K(|V| + |E|)F)), where (K) is the number of attention heads, (|V|) is the number of nodes, (|E|) is the number of edges, and (F) is the hidden feature dimension. Since the microscopic graph only contains three distress nodes within each pavement-section supernode and the macroscopic graph is sparsified by distance, traffic-correlation, and structural-continuity thresholds, the graph structure remains sparse. Therefore, the additional computational burden introduced by the dual-layer graph structure and physical constraints is acceptable for offline pavement condition assessment and maintenance strategy classification.

4.4 Evaluation Metrics for Prediction Models

To comprehensively evaluate the dual performance of the proposed DLPC-GNN in continuous physical state evolution and discrete maintenance decision-making, this study constructs a rigorous evaluation metric system from two independent but complementary perspectives: regression and classification.

4.4.1 Regression Metrics for Physical State Evolution

For the continuous physical variables in the predicted future distress evolution graph $\hat{G}_{t+\Delta t}$, the mean absolute error (MAE) and root mean square error (RMSE) are selected as regression metrics for prediction accuracy evaluation and baseline comparison. Their mathematical expressions are given as follows:

$$\mathrm{MAE} = \frac{1}{M \cdot \Delta t} \sum_{t'=t+1}^{t+\Delta t} \sum_{i=1}^{M} \left| \hat{y}_i^{t'} - y_i^{t'} \right| \tag{32}$$

$$\mathrm{RMSE} = \sqrt{\frac{1}{M \cdot \Delta t} \sum_{t'=t+1}^{t+\Delta t} \sum_{i=1}^{M} \left(\hat{y}_i^{t'} - y_i^{t'} \right)^2} \tag{33}$$

where M is the total number of monitored pavement sections, namely supernodes, in the macroscopic road network; Δt is the prediction time step or time interval; and $\hat{y}_i^{(t')}$ and $y_i^{(t')}$ denote the predicted and true values of the key physical indicator, such as deflection response, for the i-th pavement section at the future time t', respectively. In this study, MAE and RMSE are calculated for the inverse-normalized continuous distress-state prediction outputs. Therefore, they are expressed in the same scale as the constructed pavement distress-state indicator. For clarity, the regression metrics reported in Table 5 are used to evaluate the continuous distress-state prediction task, whereas Recall is used only for the independent maintenance strategy classification task.

Table 5: Comparison results of different models.

Model	MAE	RMSE	Recall
SVR	6.5142	11.0168	0.5514
DTR	5.9821	11.7433	0.6963
RFR	4.3135	8.0284	0.6459
GBR	4.1629	9.4943	0.7841
CNN	6.1477	11.9996	0.5294
LSTM	4.5807	8.5625	0.6944
GNN	3.2678	5.882	0.7909
DLPC-GNN	2.7755	4.6229	0.8877

Note: SVR = support vector regression; DTR = decision tree regression; RFR = random forest regression; GBR = gradient boosting regression; CNN = convolutional neural network; LSTM = long short-term memory network; GNN = graph neural network; DLPC-GNN = Dual-Layer Progressive Physics-Constrained Graph Neural Network.

In structural health monitoring, MAE intuitively reflects the average deviation of deterioration trend prediction. RMSE, due to the squared error term, imposes a stronger penalty on extreme prediction errors that deviate from mechanical rationality. Therefore, RMSE is particularly suitable for examining whether the physical constraints, such as the bounded deflection evolution model embedded in the physics-informed neural network (PINN) framework, effectively prevent non-physical divergence in long-term prediction.

4.4.2 Classification Metrics for Maintenance Strategy Classification

For the discrete maintenance decision category $\hat{y}_{maintenance}$ output by the network, the applicability of the model in practical engineering scenarios must be evaluated by considering the natural imbalance in pavement distress distributions. For example, severely deteriorated samples requiring structural rehabilitation are far fewer than healthy samples requiring only routine inspection.

Although recall at top K is commonly used in information retrieval to evaluate retrieval hit rates, simply pursuing the overlap ratio of high-frequency distressed areas is insufficient for cost-sensitive structural maintenance decision-making. To comprehensively evaluate the balance between false alarms, which may cause maintenance resource waste, and missed detections, which may lead to sharply increased structural failure costs, this study uses Recall as the primary classification metric in the baseline comparison (Table 5), while Accuracy, Precision, Recall, and Macro-F1 score are used in model-development diagnostics and ablation analyses.

For class c, Precision and Recall are defined as:

$$\text{Precision}_c = \frac{TP_c}{TP_c + FP_c} \tag{34}$$

$$\text{Recall}_c = \frac{TP_c}{TP_c + FN_c} \tag{35}$$

The Macro-F1 score is defined as:

$$\text{Macro} - F1 = \frac{1}{K}\sum_{c=1}^{K}\frac{2 \times \text{Precision}_c \times \text{Recall}_c}{\text{Precision}_c + \text{Recall}_c} \tag{36}$$

where K is the total number of defined maintenance decision categories, including preventive maintenance and corrective maintenance; TP_c, FP_c, and FN_c represent the numbers of true positive, false positive, and false negative samples identified for the c-th maintenance decision category, respectively.

Since Macro-F1 independently calculates the F1 score of each category and then takes their arithmetic mean, it treats all categories equally. This metric provides a stringent evaluation of whether DLPC-GNN can accurately recommend proactive maintenance strategies when capturing early-stage hydro-mechanical deterioration features, such as moisture infiltration along microcracks before large-scale voiding occurs. Therefore, Macro-F1 is particularly important for ensuring the reliability of maintenance decision-making and the economic evaluation of maintenance strategies.

5 Results

To systematically evaluate the effectiveness and reliability of the proposed DLPC-GNN in pavement structural distress prediction and maintenance decision-making, this study conducts a comprehensive validation from four perspectives: prediction accuracy, physical consistency, contribution of model components, and robustness. First, comparative experiments with multiple mainstream models are performed to verify the accuracy advantage of DLPC-GNN in multi-task prediction. Second, the physical rationality of the model outputs is analyzed from the perspectives of mechanical boundary constraints and hydro-mechanical coupling mechanisms. Third, ablation experiments are conducted to quantitatively evaluate the independent contributions of the Dual-Layer architecture and physical constraints. Finally, the generalization capability and stability of the model are examined under non-ideal conditions, including small-sample scenarios and noise interference.

5.1 Baseline Comparison of Prediction Accuracy

To verify the performance advantage of DLPC-GNN in distress-state prediction and maintenance decision-making, several representative methods are selected as baseline models, including conventional machine learning models, deep learning models, and graph neural network models without physical constraints. The models are comprehensively evaluated from two perspectives: regression tasks, including deflection value and crack area prediction, and classification tasks, namely maintenance strategy prediction.

For the continuous distress-state regression task, mean absolute error (MAE) and root mean squared error (RMSE) are adopted as evaluation metrics. These metrics are calculated from the inverse-normalized prediction outputs and therefore correspond to the scale of the continuous distress-state indicator. For the independent maintenance strategy classification task, Recall is used to measure the model's ability to identify key maintenance categories. The comparison results are shown in Table 5.

Before presenting the quantitative comparison, the generation process of the numerical results in Table 5 is further clarified. The reported metrics were not calculated directly from the raw inspection records. Instead, the raw multi-source data were first assigned to the corresponding pavement monitoring sections and temporally synchronized according to the preprocessing procedure described in Section 4.2. The synchronized inspection variables were then converted into the heterogeneous node feature tensors, microscopic physics-driven adjacency matrices, macroscopic spatial topology matrices, physical boundary-condition tensors, and maintenance strategy labels defined in Section 4.2.1. These processed tensors constitute the intermediate graph-sequence samples used as the direct input of DLPC-GNN.

For a fair comparison, all baseline models were trained and tested using the same training/testing split and the same normalized feature set. For models that cannot directly process graph-structured inputs, the section-level feature tensors were reshaped into the corresponding tabular, sequential, or grid-like input forms while keeping the sample partition unchanged. During testing, each model produced the predicted distress-state variables and maintenance strategy category for the same testing samples. The regression metrics in Table 5 were calculated from the deviation between the predicted and measured physical-state variables, while the classification metric was calculated from the predicted and recorded maintenance strategy labels. Therefore, Table 5 reflects the performance comparison under a unified preprocessing, sample partitioning, and evaluation protocol, rather than results obtained from different data-processing pipelines.

The Convolutional Neural Network (CNN) baseline was further checked to ensure the fairness of the comparison. It should be noted that the CNN model in this study was not used for raw pavement image recognition, but for the processed section-level heterogeneous tensors constructed from multi-source inspection records. Its architecture and hyperparameters, including the number of convolutional filters, kernel size, dropout rate, learning rate, and batch size, were tuned on the validation set. The relatively lower performance of CNN is mainly because the input variables in this task, such as material parameters, deflection responses, moisture states, traffic loads, rainfall boundary conditions, and graph-topological information, do not naturally form a regular Euclidean grid with strong local translation-invariant patterns. Therefore, reshaping these heterogeneous engineering features into convolutional inputs may weaken their physical and spatial-topological meanings. In contrast, the random forest baseline is more robust for heterogeneous tabular features under limited-sample conditions, which explains why it outperforms CNN in Table 5. This result should not be interpreted as CNN being generally inferior for pavement distress detection, but rather as evidence that conventional CNNs are less suitable for the graph-sequence prediction task considered in this study.

To further discuss the performance consistency of different models in long-horizon prediction tasks, the prediction results from the 13th to the 18th month, namely a future six-month prediction window, are compared among the above models, as shown in Fig. 5.

Overall, DLPC-GNN achieves the best performance across all evaluation metrics. Compared with the average results of conventional machine learning models, including support vector regression (SVR), decision tree regression (DTR), random forest regression (RFR), gradient boosting regression (GBR), DLPC-GNN reduces MAE by approximately 47.1% and RMSE by approximately 51.5%. This indicates that the proposed model can more effectively extract high-dimensional nonlinear features in complex pavement distress evolution scenarios and significantly reduce prediction errors in continuous physical states. Compared with the convolutional neural network-based model, DLPC-GNN further improves prediction accuracy. This improvement is mainly attributed to the fact that DLPC-GNN does not rely solely on local pixel-level features, but explicitly models the spatial topological relationships and evolutionary dependencies among cracking, moisture-induced damage, and surface deterioration, thereby providing a more accurate representation of the distress propagation process.

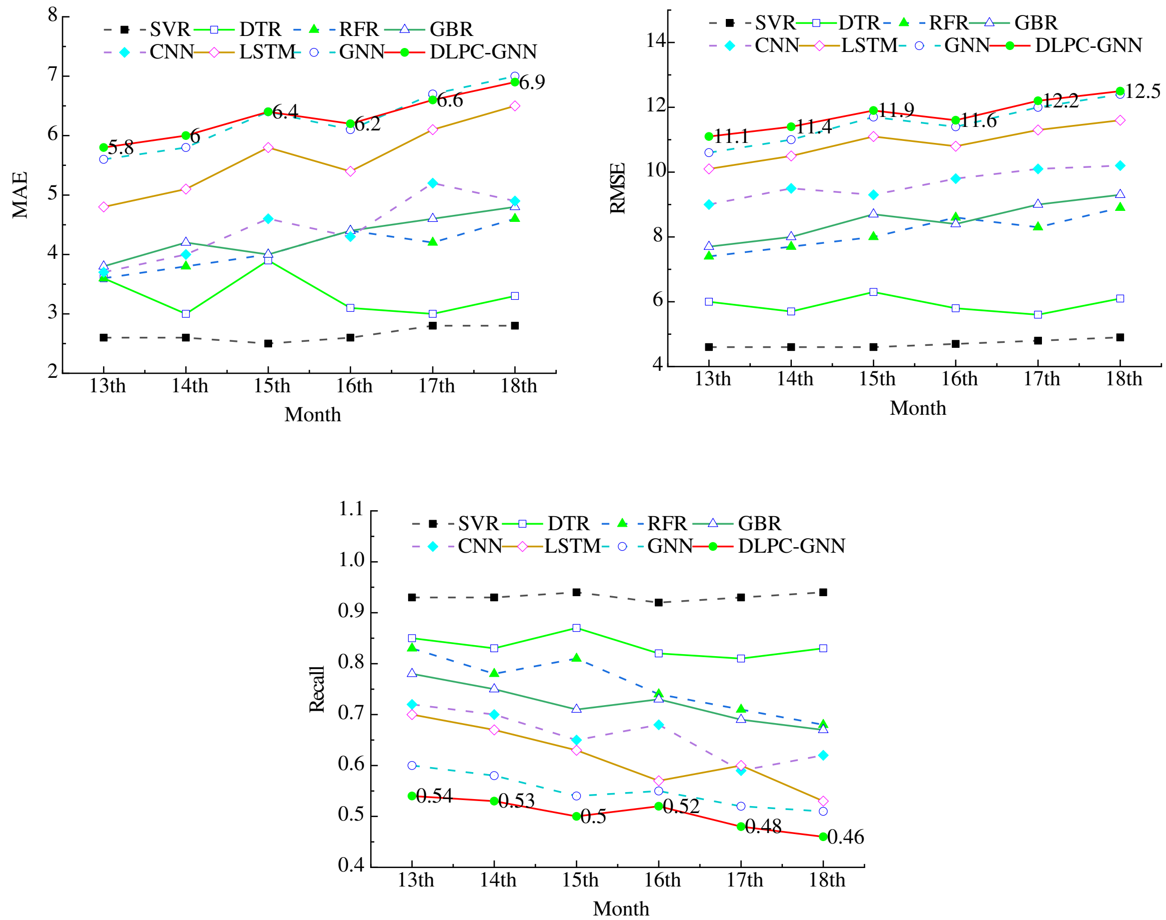

Figure 5: Monthly comparison of prediction performance.

More importantly, compared with the purely data-driven graph neural network (GNN), DLPC-GNN reduces MAE by 15.1% and improves Recall by approximately 12.2%. This result demonstrates that the introduction of physical constraints and the Dual-Layer progressive graph structure can effectively suppress the overfitting tendency of purely data-driven models in complex nonlinear scenarios and enhance the model's ability to represent real deterioration mechanisms. In other words, the performance advantage of DLPC-GNN does not simply originate from graph-structure modeling, but from the joint contribution of physics-informed edge initialization, macroscopic road-network topology awareness, and multi-source physical constraints.

In addition, the monthly prediction performance comparison shown in Fig. 5 indicates that DLPC-GNN exhibits a significantly lower error growth rate than other models in long-term prediction tasks. In particular, even when the prediction horizon is extended, DLPC-GNN maintains relatively low MAE and RMSE values, demonstrating superior temporal stability and long-horizon prediction capability. This suggests that the physical constraint terms play a regularization-like role in long-sequence prediction, limiting the deviation of model outputs from structural deterioration laws and thereby improving the reliability of the model in practical maintenance decision-making.

5.2 Consistency Verification of Physical Evolution Laws

Compared with conventional data-driven models, DLPC-GNN introduces multi-source physical constraints, enabling the model to maintain high prediction accuracy while achieving improved physical interpretability. This section verifies the physical consistency of the model outputs from the perspective of hydro-mechanical coupling mechanism capture. Considering the complex hydro-mechanical coupling among crack propagation, water infiltration, and base-course voiding during pavement structural deterioration, this study further analyzes the variation patterns of the edge weights, namely attention coefficients, learned by the model in the microscopic distress-oriented physical association graph.

It should be noted that the rainfall-related variables are involved in the physics-informed edge initialization. Therefore, the following edge-weight response analysis is not intended to serve as an independent mechanistic validation, but rather as a physical plausibility check of whether the learned attention weights after model training remain directionally consistent with the imposed hydro-mechanical priors and do not produce physically contradictory trends.

Specifically, the evolution edge weight $w_{A\to C}$ and the deterioration edge weight $w_{C\to B}$ are extracted, and their response characteristics with respect to rainfall intensity and hydrodynamic pressure are analyzed. The results are shown in Fig. 6.

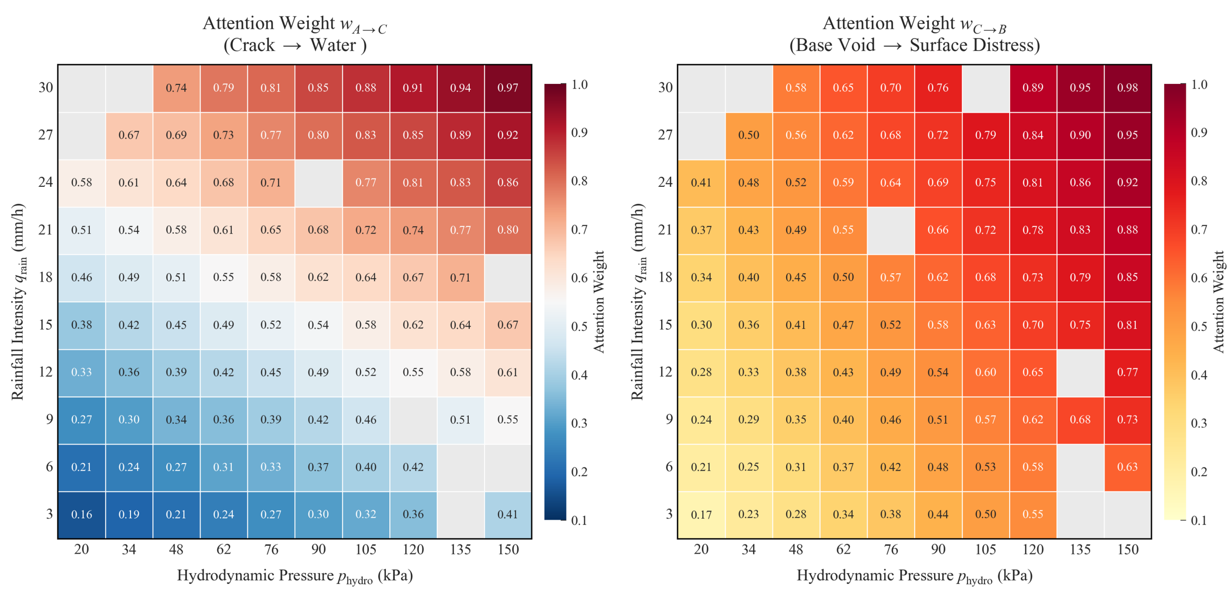

Figure 6: Response characteristics of microscopic distress edge weights under rainfall intensity and hydrodynamic pressure.

The results show that the microscopic distress edge weights learned by DLPC-GNN exhibit clear physical consistency with variations in rainfall intensity and hydrodynamic pressure. For the evolution edge $w_{A\to C}$, which represents crack-induced structural moisture damage, the edge weight increases significantly with rainfall intensity. Across the evaluated rainfall range, the average evolution-edge weight increases with rainfall intensity. This indicates that, with increasing rainfall intensity, crack openings gradually become preferential seepage channels for water entering the pavement structure, thereby significantly strengthening the inducing effect of cracking on structural moisture-induced damage. This result is consistent with the understanding from unsaturated seepage theory that an increase in rainfall boundary flux enhances internal moisture content and seepage driving force within the structure.

For the deterioration edge $w_{C\to B}$, which represents surface deterioration induced by structural moisture damage, the edge weight is more sensitive to hydrodynamic pressure. When hydrodynamic pressure increases from 20 to 150 kPa, the average value of $w_{C\to B}$ increases from approximately 0.290 to 0.836, corresponding to a relative increase of approximately 188.3%. In particular, the edge weight rises rapidly in the medium-to-high hydrodynamic pressure range. This suggests that once moisture accumulation, loosening, or local voiding has occurred inside the pavement structure, transient hydrodynamic pressure induced by vehicular loading significantly enhances base-course scouring, pumping, and weakening of structural bearing capacity, thereby accelerating the development of surface deterioration.

It should be emphasized that the hydrodynamic pressure-related edge weight does not represent a monthly average of an instantaneous pressure response. Instead, it represents the aggregated intensity of repeated short-duration hydrodynamic impacts within the observation window. Therefore, the integration of transient hydrodynamic pressure with fatigue and deflection degradation is physically rational because the former acts as an intra-window driving factor, while the latter represents the accumulated structural consequence updated between graph snapshots.

A further comparison of the two types of edge weights shows that $w_{A\to C}$ is mainly governed by rainfall intensity, whereas $w_{C\to B}$ is mainly controlled by hydrodynamic pressure. This indicates that DLPC-GNN can distinguish the dominant physical factors at different stages of distress evolution: rainfall primarily drives the "cracking–moisture damage" process, whereas hydrodynamic pressure mainly drives the "moisture damage–surface deterioration" process. It should be noted that the gray blank regions in the figure represent invalid operating conditions, missing-data conditions, or abnormal combinations not included in the statistical analysis. These regions are excluded from the calculation of means and relative increments to avoid interference from invalid samples in judging the edge-weight variation trends. Overall, physics-informed edge initialization and multi-source physical constraints enable the model to learn distress propagation paths with explicit engineering significance, thereby improving the interpretability and engineering credibility of the prediction results. The temporal relationship between rainfall intensity and the learned microscopic edge weights is further shown in Fig. 7.

The results further show that the attention edge weights learned by DLPC-GNN exhibit clear temporal response characteristics during rainfall events. Before rainfall begins, the edge weights remain generally low. As rainfall intensity increases and the wetting degree of the pavement structure rises, both the evolution edge and deterioration edge weights increase significantly and reach peak values during heavy rainfall periods. Among them, the evolution edge representing crack-induced water infiltration responds more rapidly to rainfall input. Its peak values are approximately 0.20, 0.28–0.30, and 0.42 during moderate rain, heavy rain, and rainstorm stages, respectively. This indicates that cracks can rapidly become preferential channels for moisture infiltration during rainfall. Meanwhile, after each rainfall pulse ends, the edge weights do not immediately return to their initial levels but instead exhibit gradual attenuation, suggesting that the structural moisture state and water migration effects induced by rainfall have a certain persistence.

From the perspective of the relationship between rainfall intensity and edge weights, when rainfall intensity is lower than approximately 30–35 mm/h, both $w_{A\to C}$ and $w_{C\to B}$ remain at relatively low levels, indicating that the distress propagation paths are not significantly activated under weak rainfall conditions. When rainfall intensity increases to approximately 40 mm/h, both edge weights show a distinct jump. Specifically, $w_{C\to B}$ increases from approximately 0.22 to 0.48, while $w_{A\to C}$ increases from approximately

0.14 to 0.27. This reflects the threshold-triggering characteristics of water infiltration and structural deterioration. As rainfall intensity further increases, both edge weights continue to rise and reach high levels in the range of 100–120 mm/h, with $w_{C\to B}$ approaching 0.90 and $w_{A\to C}$ reaching approximately 0.80. This indicates that intense rainfall not only enhances crack-induced infiltration but also amplifies the effect of water infiltration on base-course voiding, pumping, and structural bearing-capacity weakening.

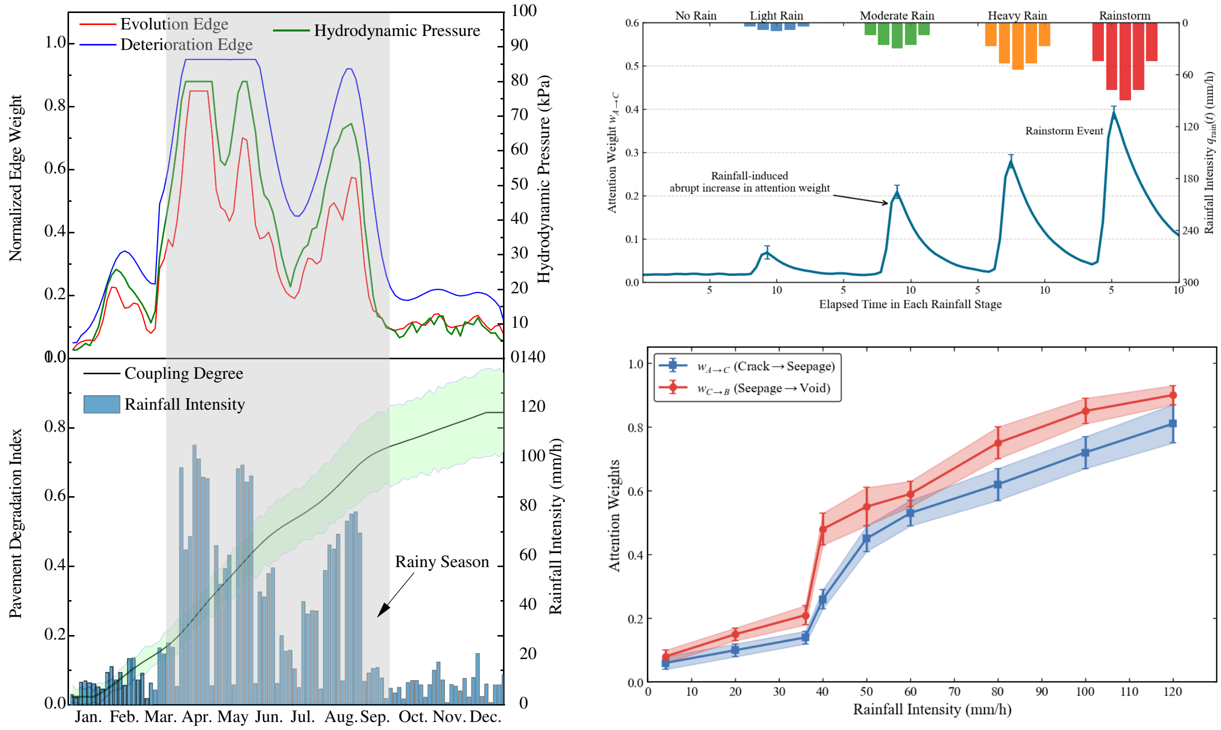

Figure 7: Relationship between rainfall intensity and learned edge weights.

Overall, the learned attention weights show trends that are directionally consistent with the expected hydro-mechanical deterioration process of "rainfall infiltration–moisture accumulation–hydrodynamic pressure enhancement–structural damage propagation". However, because rainfall-related variables are also used in the physics-informed edge initialization, this result should be interpreted as a physical plausibility check rather than independent mechanistic validation. This clarification has been added to avoid over-interpreting the edge-weight response analysis. Further independent mechanistic validation using controlled laboratory tests or external field datasets will be considered in future work to more rigorously quantify the causal relationship between rainfall infiltration, hydrodynamic pressure, and pavement distress propagation. In addition, the attention pooling weights used for microscopic-to-macroscopic aggregation are learned in a data-driven manner. Although the ablation study indicates that attention pooling improves prediction performance compared with mean pooling, the present study does not further conduct scenario-specific analysis of pooling weights under rainy or heavy-traffic conditions. Therefore, the interpretability of the attention pooling module should be regarded as limited, and its physical rationality requires further validation using targeted engineering scenarios in future work.

5.3 Ablation Study on Network Architecture

To further verify the contribution of each key module in DLPC-GNN to prediction performance and physical consistency, ablation experiments are conducted under the same dataset partition, training epochs, optimizer, and hyperparameter settings. The ablation study follows a "single-variable removal" principle, where only one core module is removed or replaced at a time and compared with the complete DLPC-GNN. The evaluation metrics include MAE and RMSE for the regression task, as well as Recall and Macro-F1 for the maintenance decision classification task. The benchmark results of the complete DLPC-GNN are MAE = 2.7755, RMSE = 4.6229, Recall = 0.8877, and Macro-F1 = 0.8794.

Ablation Analysis of Network Structure Modules

As shown in Table 6, the complete DLPC-GNN achieves the best results across all metrics. After removing the macroscopic road-network spatial topology layer, MAE increases from 2.7755 to 3.2631, representing an increase of 17.57%; RMSE increases from 4.6229 to 5.5527, representing an increase of 20.11%; and Recall decreases from 0.8877 to 0.8246, corresponding to a relative decrease of 7.11%. This result indicates that relying only on the microscopic distress graph can characterize the local coupling relationships among cracking, moisture-induced damage, and surface deterioration, but it is insufficient for capturing regional deterioration propagation among adjacent pavement sections driven by traffic flow, structural continuity, and hydrological environment.

Table 6: Ablation results of network structure modules.

Model	MAE	RMSE	Recall	Macro-F1
Complete DLPC-GNN	2.7755	4.6229	0.8877	0.8794
Without macroscopic topology layer	3.2631	5.5527	0.8246	0.8143
Mean pooling instead of attention pooling	3.0472	5.2468	0.8509	0.8392
Random adjacency instead of physics-informed edge initialization	3.1186	5.3194	0.8421	0.8328
Without progressive training	3.0094	5.1286	0.8584	0.8475

When mean pooling is used instead of attention pooling, MAE and RMSE increase by 9.79% and 13.50%, respectively. This indicates that different distress nodes do not contribute equally when microscopic distress features are aggregated into macroscopic pavement-section supernodes. Attention pooling can adaptively highlight critical deterioration nodes, such as crack propagation and moisture-induced voiding, and is therefore more suitable than simple mean pooling for modeling complex pavement distress evolution.

When a random adjacency matrix is used instead of physics-informed edge initialization, MAE and RMSE increase by 12.36% and 15.07%, respectively, while Recall decreases by 5.14%. This demonstrates that the physical edge weights constructed based on the Richards equation, Paris law, and hydro-mechanical coupling mechanism are not merely prior decorations. Rather, they provide reasonable information propagation paths for the graph neural network at the early stage of training, enabling the model to converge more rapidly toward parameter regions consistent with engineering mechanisms.

After removing progressive training, the model performance also deteriorates, with MAE increasing by 8.43% and RMSE increasing by 10.94%. This indicates that when physical constraints and data-driven loss coexist, direct end-to-end training is more susceptible to the influence of a non-convex loss landscape. By contrast, the proposed training strategy of "data warm-up–physical-rule introduction–full-parameter fine-tuning" improves optimization stability and prevents the model from prematurely falling into local optima.

The ablation results of different physical constraint terms are presented in Table 7. Further analysis of the contributions of different physical constraint terms shows that after removing all physical constraints, the RMSE of the model increases from 4.6229 to 6.0918, corresponding to an increase of 31.77%; Recall decreases from 0.8877 to 0.8189, corresponding to a relative decrease of 7.75%. This indicates that multi-source physical constraints not only improve the prediction accuracy of continuous deflection responses but also enhance the model's ability to identify critical maintenance categories.

Table 7: Ablation results of physical constraint terms.

Model Variant	MAE	RMSE	Recall	Macro-F1	Physical Residual	Boundary Violation Rate of Material Parameters/%
Complete DLPC-GNN	2.7755	4.6229	0.8877	0.8794	0.036	0.8
Without mechanical response constraint	3.0918	5.5964	0.8645	0.8539	0.091	2.7
Without material boundary constraint	2.9612	5.1875	0.8721	0.8625	0.064	9.6
Without evolution logic constraint	3.1546	5.7043	0.8438	0.8317	0.118	3.4
Without all physical constraints	3.3719	6.0918	0.8189	0.8064	0.156	12.8

After removing the mechanical response constraint, RMSE increases by 21.06%, and the long-term deflection prediction curve shows a clear upward divergence trend at later prediction stages. This indicates that the mechanical response constraint can effectively suppress non-physical divergence in long-term prediction. After removing the material boundary constraint, the material parameter boundary violation rate increases from 0.8% to 9.6%, demonstrating that this constraint mainly acts on the latent variable space of the model, ensuring that the learned equivalent physical features, such as modulus and Poisson's ratio, remain within engineering-reasonable ranges. After removing the evolution logic constraint, Recall and Macro-F1 decrease most significantly, by 4.95% and 5.42%, respectively. This suggests that the evolution logic constraint plays an important role in maintaining the continuity of distress propagation paths and the stable discrimination of maintenance decision categories.

Overall, the macroscopic topology layer mainly improves the model's ability to capture regional distress propagation. Physics-informed edge initialization enhances the engineering rationality of microscopic distress relationship modeling. Attention pooling improves multi-scale feature aggregation, while the physical constraint terms improve the stability and interpretability of the model from the perspectives of mechanical boundaries, material parameters, and evolution paths. Therefore, the performance advantage of DLPC-GNN does not arise from a single module, but from the synergistic effect of the Dual-Layer graph structure, physical priors, and progressive optimization.

5.4 Robustness under Non-Ideal Data Conditions

In practical pavement inspection, multi-source detection data are often subject to non-ideal conditions, such as insufficient samples, input noise, and partial feature missing, due to inspection cost, equipment errors, traffic control constraints, and meteorological disturbances. To further verify the stability and generalization capability of DLPC-GNN in engineering applications, this study conducts comparative experiments from three perspectives: small-sample generalization, noise resistance, and robustness to feature missing.

The comparison models include the purely data-driven GNN, long short-term memory network (LSTM), and random forest regression model, namely RFR. All models adopt the same training-set partition strategy and evaluation metric system, with a focus on comparing the degradation trends of RMSE, MAE, and Recall under non-ideal data conditions.

5.4.1 Small-Sample Generalization Capability

To simulate the shortage of labeled samples in practical engineering, 100%, 80%, 50%, and 20% of the training data are selected for model training, and all models are evaluated on the same testing set. The experimental results show that as the training data ratio decreases, the prediction errors of all models increase. However, the performance degradation of DLPC-GNN is significantly smaller than that of the other models. The RMSE, MAE, and Recall results under different training data ratios are summarized in Table 8.

Table 8: RMSE under different training data ratios.

Training Ratio (%)	**DLPC-GNN RMSE**	**GNN RMSE**	**LSTM RMSE**	**RFR RMSE**
100	4.6229	5.882	8.5625	8.0284
80	5.01	6.52	9.73	9.43
50	5.39	7.58	11.84	12
20	5.82	8.74	14.6	15.25
Training ratio (%)	DLPC-GNN MAE	GNN MAE	LSTM MAE	RFR MAE
100	2.7755	3.2678	4.5807	4.3135
80	2.912	3.58	5.09	4.93
50	3.116	4.12	6.2	6.35
20	3.376	4.81	7.55	7.96
Training ratio (%)	DLPC-GNN Recall	GNN Recall	LSTM Recall	RFR Recall
100	0.8877	0.7909	0.6944	0.6459
80	0.875	0.761	0.641	0.592
50	0.852	0.706	0.572	0.503
20	0.823	0.642	0.489	0.421

When the training data ratio decreases from 100% to 20%, the RMSE of DLPC-GNN increases from 4.6229 to 5.8200, corresponding to an increase of 25.9%. In contrast, the RMSE values of GNN, LSTM, and RFR increase by 48.6%, 70.5%, and 90.0%, respectively. Meanwhile, the Recall of DLPC-GNN decreases from 0.8877 to 0.8230, corresponding to a relative decrease of 7.3%, which is much lower than the decreases of GNN and RFR, namely 18.8% and 34.8%, respectively. These results indicate that when the number of samples is insufficient, DLPC-GNN does not rely entirely on statistical correlations in the data. Instead, it can maintain reasonable information propagation paths through physics-informed edge initialization and multi-source physical constraints, thereby alleviating overfitting under small-sample conditions.

From the perspective of deep neural network training mechanisms, purely data-driven models are prone to insufficient feature representation and unstable parameter estimation when the number of samples decreases. By contrast, the Richards equation, Paris law, and bounded deflection evolution model embedded in DLPC-GNN provide additional structural priors for the network, enabling the model to maintain a relatively stable prediction trend even in low-sample regimes.

5.4.2 Noise Resistance Analysis

To evaluate the sensitivity of different models to inspection errors, Gaussian noise with a mean value of 0 is added to the input features. The noise levels are set to 0%, 5%, 10%, 20%, and 30%. The noise is applied to key input features, including IRI, permeability coefficient, deflection value, texture depth, and crack area. The model performance under different input noise levels is reported in Table 9.

Table 9: RMSE under different noise levels.

Noise level (%)	DLPC-GNN RMSE	GNN RMSE	LSTM RMSE	RFR RMSE
0	4.6229	5.882	8.5625	8.0284
5	4.95	6.31	9.44	8.83
10	5.23	6.96	10.86	10.16
20	5.68	7.92	12.77	12.25
30	6.14	9.05	15.01	14.72
Noise level (%)	**DLPC-GNN Recall**	**GNN Recall**	**LSTM Recall**	**RFR Recall**
0	0.8877	0.7909	0.6944	0.6459
5	0.879	0.768	0.66	0.61
10	0.864	0.734	0.603	0.548
20	0.839	0.689	0.539	0.474
30	0.812	0.631	0.462	0.395

The results show that as the noise level increases, the RMSE values of all models increase. However, DLPC-GNN exhibits the mildest error growth. When the noise level reaches 30%, the RMSE of DLPC-GNN increases from 4.6229 to 6.1400, corresponding to a relative increase of 32.8%. By contrast, the RMSE values of GNN, LSTM, and RFR increase by 53.9%, 75.3%, and 83.3%, respectively. For the classification task, the Recall of DLPC-GNN decreases from 0.8877 to 0.8120, representing a decrease of only 8.5%, whereas GNN and RFR decrease by 20.2% and 38.8%, respectively.

These results indicate that physical constraints play a regularization-like role during model training. On the one hand, the mechanical response constraint prevents the predicted deflection values from deviating from the mechanically reasonable range of the pavement structure. On the other hand, the evolution logic constraint suppresses abnormal edge-weight perturbations caused by noise, maintaining the continuity of distress propagation paths. Therefore, even when the input features are contaminated by noise, DLPC-GNN can still maintain strong prediction stability.

5.4.3 Robustness under Multi-Source Feature Missing Conditions

Considering that partial sensor failure, local GPR data loss, or incomplete meteorological boundary records may occur during practical inspection, this study further sets random input feature missing ratios of 0%, 10%, 20%, 30%, and 40%. A masking mechanism is used to process missing features. This experiment is designed to evaluate the performance retention capability of the model under incomplete multi-source information conditions. The robustness results under different feature-missing ratios are summarized in Table 10.

Table 10: RMSE under different feature missing ratios.

Missing Ratio (%)	DLPC-GNN RMSE	GNN RMSE	LSTM RMSE	RFR RMSE
0	4.6229	5.882	8.5625	8.0284
10	5.05	6.47	9.7	9.2
20	5.37	7.34	11.4	11.2
30	5.86	8.55	13.6	13.8
40	6.48	10.13	16.1	16.7
Missing ratio (%)	**DLPC-GNN Recall**	**GNN Recall**	**LSTM Recall**	**RFR Recall**
0	0.8877	0.7909	0.6944	0.6459
10	0.873	0.75	0.638	0.584
20	0.852	0.69	0.562	0.501
30	0.824	0.628	0.485	0.427
40	0.791	0.552	0.403	0.346

The results show that when the feature missing ratio reaches 40%, the RMSE of DLPC-GNN increases from 4.6229 to 6.4800, corresponding to an increase of 40.2%. In contrast, the RMSE values of GNN, LSTM, and RFR increase by 72.2%, 88.0%, and 108.0%, respectively. This indicates that DLPC-GNN has stronger tolerance to multi-source feature missing.

This robustness can be attributed to three factors. First, the Dual-Layer graph structure compensates for local feature missing through information propagation among adjacent nodes. Second, the macroscopic road-network topology layer uses spatial correlations among adjacent pavement sections to correct section-level states. Third, the physical constraint terms further reduce the possibility of non-physical predictions under incomplete input conditions.

In summary, DLPC-GNN exhibits smaller performance degradation under three types of non-ideal data conditions: small samples, strong noise, and feature missing. Its robustness advantage mainly originates from three aspects. First, physics-informed edge initialization provides graph neural networks with information propagation channels consistent with distress evolution mechanisms. Second, the macroscopic road-network topology layer enhances the model's ability to compensate for missing information by exploiting spatial correlations. Third, the multi-source physics-constrained loss function effectively suppresses noise-induced interference. Therefore, DLPC-GNN is more suitable for practical pavement maintenance scenarios involving incomplete inspection data, significant environmental disturbances, and insufficient sample annotations.

6 Discussion

This study addresses the challenges of multi-source inspection data fusion, insufficient representation of distress propagation mechanisms, and limited interpretability in asphalt pavement distress prediction and maintenance strategy classification. The proposed Dual-Layer Progressive Physics-Constrained Graph Neural Network (DLPC-GNN) employs graph structures as the representation framework for pavement distress states. At the microscopic level, a physical association graph among cracks, structural moisture-induced damage, and surface deterioration is constructed to describe local hydro-mechanical coupling mechanisms. At the macroscopic level, a road-network topology graph integrating spatial distance, traffic-flow correlation, and structural continuity is established to represent regional distress propagation among pavement sections. In this way, the proposed model enables multi-scale modeling of pavement distress evolution from local physical coupling to regional spatial propagation.

The introduction of physical priors further improves the interpretability of the proposed graph-learning framework. Specifically, the Richards equation for unsaturated seepage, the Paris law for fatigue crack propagation, the hydrodynamic pressure model, and the bounded deflection evolution model are incorporated into physics-informed edge initialization and auxiliary physical constraints. In addition, a multi-source physics-constrained loss function is constructed by incorporating mechanical response constraints, material boundary constraints, and evolution logic constraints. These designs help constrain the model outputs within physically reasonable ranges and reduce the risk of purely data-driven fitting that may contradict engineering deterioration mechanisms.

The experimental results show that DLPC-GNN effectively improves asphalt pavement distress-state prediction and maintenance strategy classification. Compared with conventional machine learning models, deep learning models, and purely data-driven graph neural networks, DLPC-GNN achieves the best performance in terms of mean absolute error (MAE), root mean squared error (RMSE), and Recall. Specifically, the MAE, RMSE, and Recall values reach 2.7755, 4.6229, and 0.8877, respectively. These results indicate that the dual-layer graph structure and physical constraint mechanism can reduce prediction errors for continuous physical states and improve the identification capability for critical maintenance categories. The monthly prediction results further show that DLPC-GNN exhibits a slower error growth rate in long-horizon prediction tasks, suggesting favorable temporal stability and stronger capability in capturing long-term deterioration trends.

The physical plausibility analysis indicates that physics-informed edge initialization and multi-source physical constraints enable the model to learn distress propagation paths that are directionally consistent with pavement deterioration mechanisms. The learned attention edge weights exhibit clear response patterns with respect to rainfall intensity and hydrodynamic pressure. The edge weight representing crack-induced structural moisture damage is mainly governed by rainfall intensity, reflecting crack infiltration and moisture migration processes. In contrast, the edge weight representing surface deterioration induced by structural moisture damage is more sensitive to hydrodynamic pressure, reflecting hydrodynamic scouring, pumping, and weakening of structural bearing capacity under traffic loading. These results suggest that DLPC-GNN is not limited to statistical data fitting, but can also distinguish the dominant factors at different stages of distress evolution. Nevertheless, because rainfall-related variables are involved in the physics-informed edge initialization, this analysis should be interpreted as a physical plausibility check rather than independent mechanistic validation.

The ablation experiments further demonstrate that the performance advantage of DLPC-GNN originates from the synergistic effect of the dual-layer graph structure, physical priors, and progressive training strategy. Removing the macroscopic road-network topology layer, replacing attention pooling with mean pooling, replacing physics-informed edge initialization with random adjacency, or removing progressive training all leads to different degrees of performance degradation. This indicates that the macroscopic topology layer helps capture regional distress propagation, attention pooling highlights critical deterioration nodes, physics-informed edge initialization provides reasonable information propagation paths, and progressive training alleviates the non-convex optimization problem caused by the introduction of physical constraints. Further ablation of physical constraint terms shows that the mechanical response constraint can suppress non-physical divergence in long-term deflection prediction, the material boundary constraint can prevent latent physical parameters from exceeding engineering-reasonable ranges, and the evolution logic constraint helps maintain the continuity of distress propagation paths and the stability of maintenance classification results.

The robustness analysis shows that DLPC-GNN maintains stronger stability under non-ideal data conditions, including small samples, noise interference, and feature missing. When the training sample ratio decreases, input noise increases, or multi-source features are partially missing, the degradation of RMSE and Recall in DLPC-GNN is smaller than that of comparison models such as GNN, LSTM, and RFR. This indicates that the physical constraint terms play a regularization-like role during training and can suppress abnormal predictions caused by noise and incomplete data. In addition, the dual-layer graph structure can compensate for locally missing features through information propagation among adjacent distress nodes and neighboring pavement sections. Therefore, the proposed model is more suitable for practical pavement inspection scenarios characterized by insufficient sample annotation, incomplete inspection data, and environmental disturbances.

Overall, the proposed DLPC-GNN provides a graph-learning framework for asphalt pavement distress prediction and maintenance strategy classification that integrates prediction accuracy, physical interpretability, and engineering robustness. Compared with conventional data-driven models that mainly rely on statistical correlations, DLPC-GNN organically integrates distress evolution mechanisms, road-network spatial topology, and deep graph learning. It can provide technical support for intelligent pavement maintenance, proactive distress identification, and maintenance-oriented decision support.

7 Conclusions

This study proposed a Dual-Layer Progressive Physics-Constrained Graph Neural Network for asphalt pavement distress prediction and maintenance strategy classification. By integrating microscopic distress association modeling, macroscopic road-network topology representation, physics-informed edge initialization, and multi-source physical constraints, the proposed framework improves prediction accuracy, physical interpretability, and robustness under non-ideal inspection-data conditions. The experimental results from the Huizhou section of the Huizhou–Shenzhen Expressway demonstrate that DLPC-GNN outperforms conventional machine learning models, deep learning models, and purely data-driven graph neural networks in both distress-state prediction and maintenance strategy classification.

Several limitations should also be acknowledged. First, the present study was validated using data from one expressway section, and further validation using field data from different climatic regions, pavement structures, and traffic loading conditions is still needed. Second, the current DLPC-GNN provides deterministic point estimates for distress-state prediction and deterministic maintenance strategy classification results, but does not explicitly quantify predictive uncertainty. In addition, although the attention pooling module improves the aggregation of microscopic distress nodes into macroscopic pavement-section supernodes, the physical rationality of the learned pooling weights has not been independently verified under typical rainy or heavy-traffic scenarios. Future work will analyze the scenario-dependent variation of attention weights to further strengthen the interpretability of the microscopic-to-macroscopic aggregation process. Future research will extend DLPC-GNN toward probabilistic and uncertainty-aware graph learning by incorporating techniques such as Bayesian graph neural networks, Monte Carlo dropout, deep ensembles, conformal prediction, or probabilistic output layers. In addition, maintenance cost, traffic impact, and life-cycle benefit analysis will be incorporated to improve its applicability in practical pavement management systems.

Acknowledgement: The authors would like to thank the Huizhou section maintenance and inspection team of the Huizhou–Shenzhen Expressway for their assistance in field data collection, pavement inspection, and engineering information organization.

Funding Statement: This research was supported by [2026 Annual School-level Science and Technology Project of Heyuan Polytechnic] under Grant No. [Hzykj202611] and the Thousand Talents Plan of Jiangxi Province (No. JXSQ2022017). The authors gratefully acknowledge this financial support.

Author Contributions: The authors confirm their contribution to the paper as follows: study conception and design: Mengyao Wang, Longji Zhu and Chen Lan; data collection and engineering information organization: Ailian Zhu and Yang Li; model development and methodology: Mengyao Wang and Longji Zhu; analysis and interpretation of results: Mengyao Wang, Longji Zhu and Chen Lan; draft manuscript preparation: Mengyao Wang and Longji Zhu; manuscript revision and supervision: Longji Zhu and Chen Lan. All authors reviewed and approved the final version of the manuscript.

Availability of Data and Materials: The data used in this study were collected from an actual highway operation, inspection, and maintenance project. Due to confidentiality restrictions associated with highway operation records, project-specific inspection data, and maintenance decision documents, the raw data cannot be made publicly available. The processed data or additional information may be made available from the corresponding authors upon reasonable request and with permission from the relevant project owner.

Ethics Approval: Not applicable. This study did not involve human participants, human data, or animal experiments.

Conflicts of Interest: The authors declare no conflicts of interest.

References

1. Sholevar N, Golroo A, Esfahani SR. Machine learning techniques for pavement condition evaluation. Autom Constr. 2022;136(5):104190. doi:10.1016/j.autcon.2022.104190.
2. Cano-Ortiz S, Lloret Iglesias L, Martinez Ruiz del Árbol P, Lastra-González P, Castro-Fresno D. An end-to-end computer vision system based on deep learning for pavement distress detection and quantification. Constr Build Mater. 2024;416:135036. doi:10.1016/j.conbuildmat.2024.135036.
3. Shang J, Zhang AA, Dong Z, Zhang H, He A. Automated pavement detection and artificial intelligence pavement image data processing technology. Autom Constr. 2024;168(2):105797. doi:10.1016/j.autcon.2024.105797.
4. Taheri A, Sobanjo J, Elwardany M. Pavement cracking prediction models based on deep learning physics-informed neural network. Transp Res Rec J Transp Res Board. 2026;2680(4):241–60. doi:10.1177/03611981251372087.
5. Jing J, Yang X, Cheng H, Feng X, Zheng H, Brilakis I, et al. A critical review on pavement distress detection using images and point clouds from visual features to geometric modeling. J Road Eng. 2025;5(4):583–606. doi:10.1016/j.jreng.2025.10.001.
6. Roberts R, Menant F, Di Mino G, Baltazart V. Optimization and sensitivity analysis of existing deep learning models for pavement surface monitoring using low-quality images. Autom Constr. 2022;140:104332. doi:10.1016/j.autcon.2022.104332.
7. Li J, Liu T, Wang X. Advanced pavement distress recognition and 3D reconstruction by using GA-DenseNet and binocular stereo vision. Measurement. 2022;201(6):111760. doi:10.1016/j.measurement.2022.111760.
8. Lin W, Li X, Han H, Yu Q, Cho YH. A novel approach for pavement distress detection and quantification using RGB-D camera and deep learning algorithm. Constr Build Mater. 2023;407(1):133593. doi:10.1016/j.conbuildmat.2023.133593.
9. Liu F, Liu J, Wang L, Al-Qadi IL. Multiple-type distress detection in asphalt concrete pavement using infrared thermography and deep learning. Autom Constr. 2024;161(7553):105355. doi:10.1016/j.autcon.2024.105355.
10. Li J, Yuan C, Wang X, Chen G, Ma G. Semi-supervised crack detection using segment anything model and deep transfer learning. Autom Constr. 2025;170(16):105899. doi:10.1016/j.autcon.2024.105899.
11. Guan T, Cai J, Wang Y, Yang W, Chang X, Han Y. Pavement pothole detection system based on deep learning and binocular vision. J Traffic Transp Eng Engl Ed. 2025;12(4):1100–23. doi:10.1016/j.jtte.2024.08.001.
12. Yang H, Cao J, Wan J, Gao Q, Liu C, Fischer M, et al. A large-scale image repository for automated pavement distress analysis and degradation trend prediction. Sci Data. 2025;12(1):1426. doi:10.1038/s41597-025-05748-5.

13. Justo-Silva R, Ferreira A, Flintsch G. Review on machine learning techniques for developing pavement performance prediction models. Sustainability. 2021;13(9):5248. doi:10.3390/su13095248.
14. Zhou Q, Okte E, Al-Qadi IL. Predicting pavement roughness using deep learning algorithms. Transp Res Rec J Transp Res Board. 2021;2675(11):1062–72. doi:10.1177/03611981211023765.
15. Chen L, Li H, Wang S, Shan F, Han Y, Zhong G. Improved model for pavement performance prediction based on recurrent neural network using LTPP database. Int J Transp Sci Technol. 2025;19(4):128–38. doi:10.1016/j.ijtst.2024.08.005.
16. Tamagusko T, Gomes Correia M, Ferreira A. Machine learning applications in road pavement management: a review, challenges and future directions. Infrastructures. 2024;9(12):213. doi:10.3390/infrastructures9120213.
17. Mansour E, Dhasmana H, Mousa MR, Hassan M. Machine learning-based technology for asphalt concrete pavement performance decision-making in hot and humid climates. Constr Build Mater. 2024;442(2):137625. doi:10.1016/j.conbuildmat.2024.137625.
18. Han C, Ma T, Chen S. Asphalt pavement maintenance plans intelligent decision model based on reinforcement learning algorithm. Constr Build Mater. 2021;299(4):124278. doi:10.1016/j.conbuildmat.2021.124278.
19. Zhu J, Yin Y, Ma T, Wang D. A novel maintenance decision model for asphalt pavement considering crack causes based on random forest and XGBoost. Constr Build Mater. 2025;477(2):140610. doi:10.1016/j.conbuildmat.2025.140610.
20. Chong D, Liao P, Fu W. Multi-objective optimization for sustainable pavement maintenance decision making by integrating pavement image segmentation and TOPSIS methods. Sustainability. 2024;16(3):1257. doi:10.3390/su16031257.
21. Zeng Q, Yang S, Xu C, Yang X, Wu Z, Shangguan L, et al. An automated pavement maintenance decision-making optimization model for sustainability of performance, cost and environment. J Clean Prod. 2026;545(13):147798. doi:10.1016/j.jclepro.2026.147798.
22. Jiang W, Luo J. Graph neural network for traffic forecasting: a survey. Expert Syst Appl. 2022;207(7):117921. doi:10.1016/j.eswa.2022.117921.
23. Ahmed SF, Kuldeep SA, Rafa SJ, Fazal J, Hoque M, Liu G, et al. Enhancement of traffic forecasting through graph neural network-based information fusion techniques. Inf Fusion. 2024;110:102466. doi:10.1016/j.inffus.2024.102466.
24. Topu MM, Anik MA, Wasi AT, Ahsan MM. Digital twin-driven pavement health monitoring and maintenance optimization using graph neural networks. arXiv:2511.02957. 2025.
25. Thawon I, Vo D, Bui TQ, Rattanamongkhonkun K, Chamroon C, Tippayawong N, et al. Physics-informed neural networks: current progress and challenges in computational solid and structural mechanics. Comput Model Eng Sci. 2026;146(2):2. doi:10.32604/cmes.2026.077044.
26. Liu T, Meidani H. Physics-informed neural networks for system identification of structural systems with a multiphysics damping model. J Eng Mech. 2023;149(10):04023079. doi:10.1061/jenmdt.emeng-7060.
27. Wang H, Rhiana F, Shi A, Lu Z, Li M, Wang T, et al. Physics-informed graph neural networks: predicting the composite mechanical behavior of clay-infilled concrete structures with morphed honeycomb configurations. Eng Struct. 2025;343:121267. doi:10.1016/j.engstruct.2025.121267.
28. Wang H, Tan PFM, Foo YZ, Owyong S, Lu Z, Chen HT, et al. Integrating graph neural networks with physics-informed loss function for mechanical response prediction of hollow concrete structures with morphed honeycomb configurations. Mater Des. 2025;251:113659. doi:10.1016/j.matdes.2025.113659.
29. Baniya S, Maity D. A comprehensive review of theoretical concepts and advancements in physics-informed neural networks with applications in structural engineering. Artif Intell Rev. 2025;59(2):49. doi:10.1007/s10462-025-11444-y.
30. Michaloglou A, Papadimitriou I, Gialampoukidis I, Vrochidis S, Kompatsiaris I. Physics-informed neural networks in materials modeling and design: a review. Arch Comput Meth Eng. 2026;33(4):5223–60. doi:10.1007/s11831-025-10448-9.
31. Neupane P, Wu S. A comprehensive review of moisture damage in asphalt mixtures: mechanisms, evaluation methods, and mitigation strategies. Constr Build Mater. 2025;471(2):140740. doi:10.1016/j.conbuildmat.2025.140740.

32. Yue X, Zheng J, Luo Y, Xie Y, Chen G, Ren D, et al. Quantitative evaluation of the effect of dynamic pore water pressure on fracture and fatigue damage of asphalt mixture based on semi-circular bending (SCB) and digital image correlation (DIC) technology. Case Stud Constr Mater. 2025;23:e05548. doi:10.1016/j.cscm.2025.e05548.
33. Zhang K, Lu H, Zhu R, Weng L, Zhou X, Kong X, et al. Study on pore structure evolution and water damage of asphalt mixture under cyclic loading. Constr Build Mater. 2024;440(1):137461. doi:10.1016/j.conbuildmat.2024.137461.
34. Wu H, Ji X, Song W, Wei J, Sun Y, Zhan Y, et al. Mechanical behaviors and meso analysis of asphalt mixtures under moisture damage induced by hydrodynamic impacts. Constr Build Mater. 2024;438(1):137048. doi:10.1016/j.conbuildmat.2024.137048.
35. Dong P, Cao X, Tang B. Research on dynamic stress and excess pore water pressure of asphalt pavement under hydraulic-mechanical coupling. Heliyon. 2024;10(4):e26011. doi:10.1016/j.heliyon.2024.e26011.
36. Sudarsanan N, Kim YR. A critical review of the fatigue life prediction of asphalt mixtures and pavements. J Traffic Transp Eng Engl Ed. 2022;9(5):808–35. doi:10.1016/j.jtte.2022.05.003.
37. Zeng Z, Richard Kim Y, Shane Underwood B, Guddati M. Asphalt mixture fatigue damage and failure predictions using the simplified viscoelastic continuum damage (S-VECD) model. Int J Fatigue. 2023;174(4):107736. doi:10.1016/j.ijfatigue.2023.107736.